

Keywords: Solar rotation, Inverse Modeling, Helioseismology

1. Introduction

The analysis of helioseismic data, carried out using various methodologies and acquired with ground- and space-based instruments, has given us a comprehensive insight into the rotation of the Sun’s interior, its temporal variations and the correlation of these variations with some of the characteristics of the solar activity.

Helioseismic techniques are typically categorized into two complementary approaches: (i) global helioseismology, which measures and interprets the p -modes eigenfrequencies, $\nu_{n,\ell,m}$, and (ii) local helioseismology, which measures and interprets the local wave field observed on the solar surface. The most commonly employed techniques in local helioseismology are the Fourier-Hankel decomposition, the ring-diagram analysis, the time-distance analysis, helioseismic holography, and direct modeling (see Gizon and Birch, 2017, for additional details).

One of the most important results derived from global helioseismic data and techniques is the characterization of the Sun’s internal rotation. Let us recall that the advection of the p -modes by the rotation lifts the degeneracy of eigenmodes with the same azimuthal order, m , within a multiplet of harmonic degree ℓ and radial order n . The functional form of the perturbation of the eigenfrequencies, the rotational frequency splittings, resulting from $\Omega(r, \theta)$, the solar rotation rate as a function of radius r and co-latitude θ , is a Fredholm integral equation of the first kind (Hansen, Cox and van Horn, 1977), namely

$$\frac{\nu_{n,\ell,+m} - \nu_{n,\ell,-m}}{2m} = \int_0^R \int_0^\pi K_{n,\ell,m}(r, \theta) \Omega(r, \theta) dr d\theta \quad (1)$$

$$= \frac{\Delta\nu_{n,\ell,m}}{2m} \pm \epsilon_{n,\ell,m} \quad (2)$$

where $\Delta\nu_{n,\ell,m}$ represents the n_{obs} observed rotational splittings, $\epsilon_{n,\ell,m}$ represents the associated observational errors, and $K_{n,\ell,m}(r, \theta)$ denotes the sensitivity functions of each splitting to the rotation rate, also known as rotational kernels. These kernels are known functions of the solar model and the mode eigenfunctions.

This set of n_{obs} integral equations, each corresponding to a distinct frequency splitting as per Equations 1 and 2, defines a classical inverse problem: these equations can be numerically inverted to infer the radial and latitudinal variation of the rotational rate from the splittings.

Regardless of which helioseismic observations and which inversion procedures were used, the inferred rotational rate within specific regions of the solar interior has revealed distinctive features. These inferences have presented inherent challenges to characterize them precisely (Thompson *et al.*, 1996; Chaplin and Basu, 2008; Schou *et al.*, 2008; Howe, 2009, 2016; Basu, 2016). The picture that has emerged is that of a solar radiative interior that rotates at ≈ 431 nHz from the

base of the convection zone ($\approx 0.71R_{\odot}$) down to $\approx 0.25R_{\odot}$, without any significant angular differential rotation. This result is consistent even when using data sets from different helioseismic instruments (Eff-Darwich and Korzennik, 2013). The difficulty in detecting and characterizing with reasonably low uncertainty the lowest-degree p -modes makes it challenging to infer the rotation rate below $\approx 0.25R_{\odot}$. One would need to reduce the observational errors of modes with $\ell < 5$ by a factor of approximately 50 to infer the general trend of the rotational rate below $\approx 0.15R_{\odot}$ (Eff-Darwich *et al.*, 2008). Hence, when using p -modes alone, it is not possible to rule out either a fast or slow rotating core. The inclusion of g -modes, modes that are highly sensitive to the solar core, would greatly improve inferences of the solar rotation in the deepest region of the Sun. Some promising yet unconfirmed attempts to detect and characterize g -modes have been carried out (Mathur *et al.*, 2008; Fossat *et al.*, 2017; Scherrer and Gough, 2019).

The same pattern of differential rotation that is observed at the solar surface is inferred within the solar convection zone ($r > 0.71R_{\odot}$), with the equator rotating faster than the poles. The outer 5% of the solar radius displays a sharp and intriguing increase in the rotation rate with depth. This near surface radial gradient decreases with latitudes, and we cannot rule out that it may even be reversed close to the poles (see for example, Korzennik, 1990; Rhodes *et al.*, 1990; Howe, 2009; Barekat *et al.*, 2014, and references therein). As in the case of the core, the p -modes that are more sensitive to the polar regions are the most difficult to characterize, namely the low azimuthal order and zonal modes. Hence, our inferences above $\approx 75^{\circ}$ in latitude are not yet reliable.

The transition region between the rigid rotation in the radiative zone and the differential rotation in the convection zone is known as the tachocline. It is characterized by a strong radial shear that might be the source of the magnetic activity of the Sun. Hence, it is essential to study its spatial distribution and temporal variability. The very precise position and thickness of the tachocline and how they vary with latitude are still a matter of debate due to the somewhat limited spatial resolution of rotation inversions, especially in the radial direction and at high latitudes, although the actual thickness is likely to be smaller than 1% of the solar radius (Corbard *et al.*, 1998). There are indications, although not confirmed, that some properties of the tachocline change with time (Howe *et al.*, 2000); what has been confirmed is that the tachocline is prolate and thicker at higher latitudes (Antia and Basu, 2011).

When a temporal mean at each depth and co-latitude is subtracted from a time series of rotational inversions, a pattern of bands of faster and slower rotation propagating from mid latitudes to the equator is revealed, and penetrates down to at least $\approx 0.9R_{\odot}$ (Vorontsov *et al.*, 2002; Basu and Antia, 2019) and maybe even a little deeper (Howe *et al.*, 2005). At higher latitudes, there are bands of faster rotation that migrate towards the poles, and penetrate the entire convection zone. Moreover there is a definite correspondence between these flows and the observed surface magnetic activity, i.e., the butterfly diagram.

In summary, global helioseismology has provided unprecedented insights into the dynamics of the Sun's interior. But, in order to improve our characterization of the regions closer to the solar core, the polar regions, and the tachocline, and in order to achieve a more precise characterization of the temporal changes of

the rotation rate, it is necessary to reduce or narrow down any biases of the data analysis (see for instance Korzennik, 2023, and references therein). Additionally, new inversion methods allow us to carry out careful comparisons of inferences and thus their reliability when using different algorithmic implementations. For these reasons, we have developed a new methodology that is quite different from those most commonly used for the inversion of rotational frequency splittings.

In Section 2, we summarize these most commonly used inversion techniques in global helioseismology, whereas in Section 3, we describe a new iterative inversion method. The performance of this iterative methodology is presented in Section 4, using various artificial data sets, followed by our conclusions, in Section 5, on this method niche and potential.

2. The Basics of Helioseismic Inversion Techniques

In practice, most inversion algorithms require discretizing the integral relations expressed by Equations 1 and 2 into a matrix form:

$$Ax = y \pm \sigma_y \quad (3)$$

where y is the vector of observables, whose elements y_i are, in the case of rotation inversions, the rotation splittings $\Delta\nu_{n,\ell,m}/2m$, and whose dimension corresponds to the size of the observed data set, n_{obs} . The vector x is the unknown corresponding model, i.e., the rotation rate, that the inversion methodology is seeking to infer. It is a vector of dimension n_{mod} , the dimension corresponding to the number of model grid points the solution is to be inferred on. The value of n_{mod} is chosen to satisfy $n_{\text{mod}} \ll n_{\text{obs}}$, hence Equation 3 is well over-constrained. The matrix A corresponds to the discretized rotational kernels and is of dimension $n_{\text{obs}} \times n_{\text{mod}}$. If we use a step-wise constant discretization of the underlying model, the elements of A are given by:

$$a_{i,j} = \int_{r_{j-1}}^{r_j} \int_{\theta_{j-1}}^{\theta_j} K_{n,\ell,m}(r,\theta) dr d\theta \quad \text{for } i = 1, n_{\text{obs}} \text{ and } j = 1, n_{\text{mod}} \quad (4)$$

Since the rotation inversion is a two-dimensional problem, let us introduce $n_{\text{mod}}^{(r)}$ and $n_{\text{mod}}^{(\theta)}$, the number of model grid points in radius and co-latitude, respectively, with, of course, $n_{\text{mod}}^{(r)} \times n_{\text{mod}}^{(\theta)} = n_{\text{mod}}$. As for the observational errors, they are assumed to be normally-distributed with zero mean and uniform variance σ_y .

Basically, two types of linear fully two-dimensional inversion techniques, plus some modifications and adaptations, have been used in global helioseismology to infer the internal rotation profile from the observed frequency splittings: the Regularized Least Squares (RLS) method and the Optimally Localized Averages (OLA) one.

The RLS approach to the inversion problem (Christensen-Dalsgaard, Hansen and Thompson, 1993; Barret, 1994) is to find, essentially through a least-squares fit, the model profile that best fits the data, subject to a smoothness penalty

term, or regularization. This is accomplished by minimizing the following functional form:

$$\|Ax - y\|^2 + \alpha\|Ly\|^2 \quad (5)$$

where an estimate of x is computed by solving this set of normal equations:

$$x = (A^T A + \alpha L^T L)^{-1} A^T y = Ty \quad (6)$$

where

$$T = (A^T A + \alpha L^T L)^{-1} A^T \quad (7)$$

The matrix L in Equation 5 corresponds to the regularization function that is introduced to lift the problem intrinsic singularity and in practice to remove the oscillatory component of the solution, resulting from the ill-conditioned nature of the problem and the effect of the noise present in the input data set (also known as noise amplification or noise magnification). As a result, the quality of the solution, in terms of error propagation and damping of undesired features, depends on the choice of L and the factor α (also known as a Lagrange multiplier). Most used regularization matrices, L , are the identity matrix, I , and finite difference matrices, such as:

$$L = \frac{1}{2} \begin{bmatrix} 1 & -1 & & & 0 \\ & 1 & -1 & & \\ & & \cdot & \cdot & \cdot \\ & & & \cdot & \cdot \\ 0 & & & & 1 & -1 \end{bmatrix} \quad (8)$$

or

$$L = \frac{1}{4} \begin{bmatrix} -1 & 2 & -1 & & & 0 \\ & -1 & 2 & -1 & & \\ & & \cdot & \cdot & \cdot & \\ & & & \cdot & \cdot & \cdot \\ 0 & & & & -1 & 2 & -1 \end{bmatrix} \quad (9)$$

By substituting y in Equation 6 by the corresponding expression in Equation 1, the solution x_j , at the grid point j is given by:

$$x_j = \int_0^R \int_0^\pi T^{(j)} K_{n,\ell,m}(r, \theta) \Omega(r, \theta) dr d\theta \quad (10)$$

namely that the product of the j^{th} row of T , $T^{(j)}$, by the rotation kernel $K_{n,\ell,m}(r, \theta)$ is nothing other than the inversion corresponding averaging kernel. The averaging kernel is the weighting function that relates the true underlying rotation profile, $\Omega(r_j, \theta_j)$ to the inferred profile, x_j , at each given depth and latitude. In the ‘‘perfect’’ case, the averaging kernels would simply be Dirac functions centered at (r_j, θ_j) . Moreover, if the errors in the input data set are uncorrelated and properly described by a normal distribution, the norm $\|T\|$, will correspond to the error propagation on the solution.

In the case of the OLA approach (Backus and Gilbert, 1968) the most used adaptation in helioseismology is the Subtractive Optimally Localized Averages (SOLA; Pijpers and Thompson, 1994). This inversion method looks for the minimization, at each j^{th} location where the inversion is carried out, of the difference between the actual averaging kernels and a target kernel, represented by a matrix $R^{(j)}$, for example a two-dimensional Gaussian or Lorentzian function. This is done minimizing the functional form

$$\|A^T T^{(j)} - R^{(j)}\|^2 + \alpha_j \|T^{(j)}\|^2 \quad (11)$$

that leads to solving the set of normal equations:

$$(AA^T + \alpha_j I)T^{(j)} = AR^{(j)} \quad (12)$$

$$T^{(j)} = (AA^T + \alpha_j I)^{-1} AR^{(j)} \quad (13)$$

Both the trade-off parameter α_j , i.e., a trade-off between resolution misfit and model variance, and the radial and latitudinal resolution of the target kernel $R^{(j)}$ must be chosen before running the inversion. The solution of the SOLA inversions at the j^{th} location is therefore given by

$$x_j = T^{(j)} y \quad (14)$$

A comparison of Equations 6 and 14 that are used to calculate the solutions in the RLS and SOLA techniques respectively, reveals that basically both inversion procedures form linear combinations of the data to derive well-localized inferences of the rotation rate at different locations within the Sun.

Let us write the matrices T in both inversion methods in terms of their singular value decomposition (SVD)

$$T = U W V^T \quad (15)$$

where W is a square diagonal matrix, that contains the singular values of matrix T , ordered in descending order. The smallest singular values are responsible for the amplification of the noise and any bias present in the data (Christensen-Dalsgaard, Hansen and Thompson, 1993). Consequently, the various inversion methods can be seen in terms of how they filter out or truncate these undesirable low singular values. Variations in the results from different inversion methodologies often arise from how these techniques handle these eigenvalues and consequently how they effectively filter the uncertainties in the data.

3. Description of the SART-Based Iterative Inversion Method

Our inversion algorithm is based on the Landweber iteration methodology (Engl *et al.*, 1996), which is a gradient method for the minimization of Equation 3, based on the following iteration scheme:

$$x_k = x_{k-1} - \beta A^T (A x_{k-1} - y) \quad (16)$$

The iteration scheme in Equation 16 is for $0 < \beta < 2/\|A\|^2$ and is none other than a linear regularization method for the problem described in Equation 3, as long as the iteration is truncated at some finite index k_{\max} .

In a more general framework (Sorzano *et al.*, 2017), Equation 16 can be written as:

$$x_k = x_{k-1} - \beta Q^{-1}(A x_{k-1} - y) \quad (17)$$

A family of different iterative reconstruction algorithms has been implemented depending on the choice of the matrix Q (Xu, Liow and Strother, 1993; McGaughey and Young, 1990). We opted to use the prescription for Q given by the Simultaneous Algebraic Reconstruction Technique (SART). SART was originally implemented to solve linear systems in image reconstruction (Anderson and Kak, 1984; van der Sluis and van der Vorst, 1990). It has since been proposed as an inversion technique for the solar internal rotation rate by Eff-Darwich *et al.* (2010).

In our implementation of the SART algorithm, the solution, x_k , after k iterations is given by

$$x_k = x_{k-1} + \beta P(y - A x_{k-1}) - \beta \alpha L^T L x_{k-1} \quad (18)$$

where the matrix P is given by

$$P = B^{-1} A^T C^{-1} \quad (19)$$

The SART algorithm calculates the diagonal matrices B and C from the summation of columns and rows of the matrix A , namely

$$B_{j,j} = \sum_{i=1}^{n_{\text{mod}}} A_{i,j} / \sigma_j^b \quad (20)$$

and

$$C_{i,i} = \sum_{j=1}^{n_{\text{obs}}} A_{i,j} / \sigma_j \quad (21)$$

The matrix B normalizes the iteration relative to the weighting given by each grid point to the data samples. The matrix C takes into account the weight of the samples of the data set. Both B and C are normalized by the uncertainties of the observables, hence, the iterative process takes into account the error distribution of the data. We added an extra parameter b to control the weight of the data errors in the computation of B , whose default value is 1, but can be, in practice, adjusted to values between 0.75 and 1.25 to modulate the effect of the uncertainties.

The matrix L in Equation 18, corresponds to that defined in Equations 8 or 9. However, it can be written more generally as:

$$L = \frac{1}{2n_{\text{nz}}} \begin{bmatrix} l_{1,1} & l_{1,2} & l_{1,3} & & & & & & & l_{1,n_{\text{mod}}} \\ & l_{2,2} & l_{2,3} & l_{2,4} & & & & & & \\ & & \cdot & \cdot & \cdot & & & & & \\ & & & \cdot & \cdot & \cdot & & & & \\ 0 & & & & & & l_{n_{\text{mod}},n_{\text{mod}}-2} & l_{n_{\text{mod}},n_{\text{mod}}-1} & l_{n_{\text{mod}},n_{\text{mod}}} & \end{bmatrix} \quad (22)$$

for $n_{\text{nz}} > 1$. Each row j ($j = 1, n_{\text{mod}}$) of the matrix L in Equation 22 represents how the solution around each model grid point p_i is smoothed or regularized, where $p_j \equiv (r_{i'}, \theta_{j'})$, and $i' = 1, n_{\text{mod}}^{(r)}$ and $j' = 1, n_{\text{mod}}^{(\theta)}$.

If for each model grid point, p_j , we set a regularization interval defined by a width in radius, $W_j^{(r)}$ and a width in co-latitude, $W_j^{(\theta)}$, the corresponding row j of L is given by:

$$\begin{aligned} l_{j,s} = -1 & \quad \text{if} \quad r(p_j) - W_j^{(r)} < r_s \leq r(p_j) + W_j^{(r)} \\ & \quad \text{and} \quad \theta(p_j) - W_j^{(\theta)} < \theta_s \leq \theta(p_j) + W_j^{(\theta)} \quad \text{for } s = 1, n_{\text{mod}} \\ l_{j,s} = 0 & \quad \text{otherwise} \end{aligned} \quad (23)$$

where we define n_{nz} as the number of non-zero values of the row $l_{j,s}$, and where $r(p_j)$ represents the radius at the model grid point p_j , while $\theta(p_j)$ represents the co-latitude at the model grid point p_j .

Moreover, we have:

$$l_{j,s} = n_{\text{nz}} \quad \text{if} \quad r(p_j) = r_s \quad \text{and} \quad \theta(p_j) = \theta_s \quad \text{for } s = 1, n_{\text{mod}} \quad (24)$$

The local regularization intervals, $W_j^{(r)}$ and $W_j^{(\theta)}$, are further parametrized in terms of depth and latitude as follows:

$$W = W_o \times (1 + f_r(1 - r/R_\odot)^{\gamma_r}) \times (1 + f_\theta(1 - \theta/(\pi/2))^{\gamma_\theta}) \quad (25)$$

where W_o , f_r , f_θ , γ_r and γ_θ are adjustable parameters, with one set for determining $W^{(r)}$ and one set for $W^{(\theta)}$.

The independent radial and latitudinal regularization intervals defined in Equations 22 to 25 allow us to study in detail the impact of different regularization schemes in the inversion procedure. On the one hand, the spatial distribution of the inversion model grid is an adjustable parameter, namely the number of grid points in both directions (i.e., the values of $n_{\text{mod}}^{(r)}$ and $n_{\text{mod}}^{(\theta)}$). On the other hand, the model grid point spacing does not need to be uniform and can be adjusted to correspond to the inversion resolution, a property that is known a posteriori by examining the averaging kernels and depends mostly on the extend of the data set (i.e., which modes are included) and the uncertainties.

After reordering terms, Equation 18 becomes:

$$x_k = (I - \beta PA - \beta \alpha L^T L)x_{k-1} + \beta Py \quad (26)$$

and since x_{k-1} can be written in terms of x_{k-2} , we have

$$x_k = (I - \beta PA - \beta \alpha L^T L)[(I - \beta PA - \beta \alpha L^T L)x_{k-2} + \beta Py] + \beta Py \quad (27)$$

Again, after reordering terms, we can write:

$$x_k = (I - \beta PA - \beta \alpha L^T L)x_{k-2} + [(I - \beta PA - \beta \alpha L^T L) + I]\beta Py \quad (28)$$

This process can be repeated for each iteration, namely:

$$x_k = (I - \beta PA - \beta \alpha L^T L)^k x_0 + [(I - \beta PA - \beta \alpha L^T L)^{k-1} + (I - \beta PA - \beta \alpha L^T L)^{k-2} + \dots + I]\beta Py \quad (29)$$

leading to:

$$x_k = (I - \beta PA - \beta \alpha L^T L)^k x_0 + \sum_{i=0}^{k-1} (I - \beta PA - \beta \alpha L^T L)^i \beta Py \quad (30)$$

that we rewrite, by introducing a matrix T , as

$$x_k = (I - \beta PA - \beta \alpha L^T L)^k x_0 + Ty \quad (31)$$

where T is given by

$$T = \sum_{i=0}^{k-1} (I - \beta PA - \beta \alpha L^T L)^i \beta P \quad (32)$$

The solution at iteration k is therefore calculated in terms of an initial estimate, x_0 , and a linear combination of the observables, i.e., the data vector, y , as per the matrix T . Note that x_0 can in principle be anything we want, and while it is often just an apriori estimate of the mean of the solution, it can be used to incorporate prior information on the solution.

For any matrix G that has all of its eigenvalues with absolute values smaller than 1, the following relationship holds

$$G^{-1} = \sum_{i=0}^{\infty} (1 - G)^i \quad (33)$$

By comparing Equation 7 and the left hand side of Equation 33, we can write

$$G = (A^T A + \alpha L^T L) \quad (34)$$

whereas from the comparison of Equation 32 and the right hand side of Equation 33 we find the following approximation

$$(1 - G)^i \approx (I - \beta PA - \beta \alpha L^T L)^i \quad (35)$$

hence, the inversion matrix for the RLS method is in fact an approximation of the truncated power expansion, up to k , defined by our SART-based iterative technique.

Unlike previous attempts to calculate the error propagation and resolution of iterative helioseismic inversions using Monte-Carlo simulations (Sudnik and Thompson, 2009), our method gives us an explicit formulation to compute both the error propagation and the averaging kernels by using the matrix T .

The choice of the optimal inversion parameters is dictated by finding the best trade-off between the error propagation $\|T\|$ and the goodness of the solution in a least squares sense, $\|Ax - y\|$. In this SART-based iterative inversion methodology, the solution depends on three primary parameters: α , β and k_{\max} the number of iterations, although besides these, the results will also depend on the choice of the regularization matrix L and the inversion model grid. In practice, we used in all cases 1500 iterations, a number that was determined to correspond to full convergence.

4. Potential of the SART-Based Iterative Inversion Methodology

The potential of this iterative technique was carefully ascertained using artificial data. To this effect, we used realistic rotational profiles, namely profiles that include a tachocline, with a solid body and differential rotation below and above it, but also other features placed either at the center or closer to the surface and at high latitudes. A precise forward computation, using rotational kernels derived from a standard model (model ‘S’; Christensen-Dalsgaard *et al.*, 1996), was carried out to produce sets of rotational splittings that cover the range of modes that can be precisely measured with modern helioseismic techniques, namely the (n, ℓ, m) set of modes resulting from fitting a 6.3 years long time series of the Helioseismic and Magnetic Imager (HMI) observations (i.e., 2304 day long or 32×72 days, see Korzennik, 2023, and references therein).

These models and computations were devised and carried out in the framework of an ongoing large collaboration to compare modern rotation inversion techniques¹. We reproduced these forward computations with our own numerical implementation down to numerical noise and used the analytical representation of one model to produce somewhat similar models for additional forward computations of artificial data sets.

The observational uncertainties of fitting a 6.3 year long time series were used to associate an uncertainty to each artificial rotational splitting, since even when inverting a noiseless artificial data set, any inverse method needs to scale the problem by the uncertainties. While the overall scaling of these uncertainties is arbitrary when inverting noiseless splittings, using uniform uncertainties would attribute more diagnostic potential to the low degree modes.

In addition to noiseless artificial splittings, sets of artificial splittings with random Gaussian noise with zero mean and a standard deviation equal to each mode uncertainty were also computed and inverted.

¹These models were devised by Dr. A. Kosovichev, and already used in a “hare and hounds” exercise back in 1998, see Appendix A of Schou *et al.* (1998), while the ongoing collaboration was initiated by the late Dr. M. Thompson and is now led by Dr. J. Christensen-Dalsgaard and should be eventually published in Christensen-Dalsgaard *et al.*, (in preparation).

Figure 1 shows two rotation profiles used to generate artificial rotational splittings, while Figure 2 shows the actual mode set in the ℓ - ν space, the corresponding noiseless splittings for each mode, and the distribution of the uncertainties.

4.1. Inversion of Noiseless Artificial Data

Figures 3 and 4 show the inferred rotational profiles when inverting noiseless artificial splittings for each model respectively. Each figure presents the inferred rotation rate using the SART-based inversion method when using two different regularizations, namely a second derivative smoothing or a variable smoothing² that is a function of depth and latitude. They also show the inferred profile when using a conventional RLS inversion methodology (Eff-Darwich and Pérez Hernández, 1997). For all three inversion methods most of the “features” of the models are recovered, although different systematic biases can be seen.

Most notably, for model 1, the values in the inner 25% radius show systematic errors larger than elsewhere and the two SART-based inferences are overall more accurate than the RLS one. The same can be seen for model 2, although the improved “sharpness” of the SART-based inferences is more obvious in this case since the model 2 rotation rate has such sharp and distinct features. Again, the SART-based inferences perform better closer to the center than the RLS, but still show systematic errors in the inner 25% radius of a different nature than the errors in the RLS inference. For both models, the SART-based inferences are more accurate than the RLS ones in the outer 75% radius and at high latitudes. This is summarized in Table 1 where the RMS of the differences with respect to the input model profile are tabulated.

The corresponding averaging kernels, for selected target locations are shown in Figures 5 to 10 for target locations near the surface, at mid depth or near the center and at low or high latitudes. Let us point out that averaging kernels, for all else equal, are independent of the values of the splittings (i.e., of rotation profile), since it is the extent of the mode set, the splittings uncertainties and the trade-off value that matters.

For most target locations the averaging kernels resulting from each inversion technique and type of regularization are somewhat dissimilar, with the largest contrast for the kernels corresponding to the deeper target locations. It is worth noting that the properties of the averaging kernels resulting from using the SART-based methodology are such that their centers of gravity are almost always very close to the target location, although the center of gravity of the main peak of that kernel can be quite displaced from that target location. This is quite different from the similar property of the averaging kernels resulting from using the RLS methodology, where the overall center of gravity of the kernels can be quite different from the target location when the kernel is not well localized at that target location. One can also see that the kernels resulting from the SART-based methodology have, when the kernel is well localized, a more narrow

²parameters of the variable regularization are $(W_o, f_r, f_\theta, \gamma_\theta, \gamma_r) = (1\text{E-}2, 99, 1, 3, 3)$ for $W^{(r)}$ and $(3.6\text{E-}2, 0, 1, 1, 3)$ for $W^{(\theta)}$.

main peak than those resulting from the RLS methodology, hence the inverted profiles are sharper, but also show more extended “wings”. In contrast, when the kernel is poorly-localized, the kernels for the SART-based methodology have very extended “wings”, while the kernels for the RLS methodology are more compact, but their center of gravity is quite offset from the target location (see Figure 9).

4.2. Inversion of Artificial Data with Random Noise

Figures 11 and 12 show the inferred rotational profiles when inverting artificial splittings with random noise, for each model respectively. As for the noiseless cases each figure presents the inferred rotation rate using the SART-based inversion method when using the same two different regularizations (a second derivative smoothing or a variable smoothing) and the inferred profile when using a conventional RLS inversion methodology. For these results, we apply a mask to hide the regions where the inversion results are unreliable, namely where the corresponding averaging kernels are not localized anywhere close to the target location.

For each combination of methodology and regularization, the inferred solutions recover the overall character of the underlying true rotation profile, but with different levels of precision at different positions and not quite the same departure from the true solution for each model. Not surprisingly, the solutions are quite good at low latitudes in the convection zone. Using a variable smoothing for regularization improves the SART-based solutions in the radiative zone, since the smoothing increases with depth and latitude.

One also notice that the SART-based solutions deviate more from the true solution at the highest latitudes, compared to the RLS solutions, but the specific nature of the solution, especially for model 2, namely, a rotation rate constant on cylinders, is better recovered with the SART-based method. Indeed the spurious oscillation seen in the RLS solution is absent in the SART-based solutions and the high latitude jet of model 2 is more clearly apparent, although somewhat displaced, for the SART-based solution with variable smoothing. The RMS of the differences with respect to the input model profile for the inversion with random noise are tabulated in Table 2.

The corresponding averaging kernels, for the same selected target locations as for the noiseless cases, are shown in Figures 13 to 18. Comparing these to the noiseless cases shows overall wider kernels, since the regularization is increased to dampen the noise. They remain well-localized for the same target locations and vice versa. When comparing these with respect to the inversion and smoothing methodology, the averaging kernels show small and subtle differences when they are well-localized and wild differences when they are not well-localized.

4.3. Effect of Regularization

To further illustrate the SART-based method, Figure 19 shows the effect of adjusting the regularization factor, α . The figure shows inferred solutions for both models, when using noiseless splittings and when using splittings with

random noise, for two values of α and the variable smoothness regularization. In all cases, decreasing α increases the smoothing and thus washes out some of the underlying profile features in exchange for reducing the noise amplification.

4.4. Inversion of Artificial Data when Using a Non-Uniform Initial Guess

One feature of our SART-based inversion methodology is the ability to start iterating from an arbitrary initial guess, one that for instance can be based on prior knowledge. To test this feature, we used several simplified variants of model 2, where we changed the width of the tachocline and removed the other “features”. We also, in one case, add a rapidly rotating core. Figure 20 shows some of these models, namely the one with a fast rotating core and two models with a slightly different tachocline width: a narrow one and a wider one.

Profiles obtained when inverting artificial noiseless splittings computed with a rapidly rotating core profile are shown in Figure 21, when using either the RLS or the SART-based method. For the SART-based method the figure shows inferences obtained when using (i) two very different values of a constant initial guess, or (ii) the known rotation profile as initial guess and three different values of the regularization factor, α . While the RLS inversion hints at a rapidly rotating core, the rotation at the center remains well underestimated. In contrast, even with only p -modes, the SART-based inversions recover the fast rotating core rate, but not its precise profile. Using the known rotation profile as an initial guess does a better job at some value of the regularization factor, but overestimates the rate at the center. The SART-based method, even with the correct initial guess and noiseless splittings, is no match to the marginal sensitivity of the p -modes to the rotation rate of the core.

Figure 22 shows rotation profiles obtained when inverting artificial noiseless splittings computed for models with various thicknesses of the tachocline. The figure compares the RLS method to the SART-based method using either a constant as the initial guess or the known rotation profile as the initial guess. In the noiseless case, the SART-based method does recover perfectly the tachocline profiles if and when the initial guess is the known rotation profile. In fact, the SART-based method does not do as well as the RLS method when using a constant as an initial guess, especially for very narrow tachoclines, but outperforms it when using the right initial guess.

Figures 23 and 24 show rotation profiles obtained when inverting artificial splittings with just a little noise or random noise corresponding to the observations and computed for some of the same models with various thicknesses of the tachocline. Once we add some random noise to the data, the benefit of using the right initial guess is unfortunately washed out, as our current implementation shows a somewhat limited immunity to noise. We plan on further investigating how to increase this noise immunity, since our SART-based method gives us a lot more flexibility in the implementation of the regularization and hence the smoothing.

5. Conclusions

We have described the new iterative rotation inversion methodology we have implemented based on the SART algorithm and have compared its performances when using artificial rotational splittings to a classical RLS inversion method. Although iterative, our implementation allows us to compute directly both the formal uncertainties on the solution, via standard error propagation, and the averaging kernels without having recourse to some form of Monte-Carlo simulation. The regularization of the inverse problem via local smoothing has been implemented in a very flexible way, using a generalized formalism. In various noiseless cases as well as realistic cases with random noise, this new technique outperforms the RLS, in precision, scope and resolution. While its immunity to noise is lower, our flexible regularization allows selective damping of this noise magnification.

The resulting averaging kernels are only slightly dissimilar to those of an RLS method where they are well-localized. In contrast, they differ by a lot where the solution is not well constrained because of poorly-localized averaging kernels.

In our current implementation, the use of some apriori information, like the sharpness of the tachocline, works remarkably well in noiseless cases, but is washed out in the presence of noise. This is an area that calls for further work, since such an iterative method could be used to improve our resolution of the tachocline. Indeed, a classical RLS combined with some form of deconvolution could be used to provide a very good initial guess to our iterative technique, once we improve the SART-based methodology noise immunity near the tachocline.

While we do not anticipate that this method will relegate the classical RLS or SOLA methods to the dustbin, using more than one technique to invert real observations can only improve the robustness of our inferences. Comparing and contrasting results obtained when using different inversion techniques allow us to better understand where these might be biased and/or unreliable, especially as we push our techniques to maximize the diagnostic potential of our observations.

Acknowledgements

Funding This work was partially supported by NASA grants 80NSSC22K0516 and NNN18ZDA001N-DRIVE to SGK and by the Spanish AEI programs PID2019-107187GB-I00 (STrESS), PID2019-104571RA-I00 (COMPACT), PID2022-139159NB-I00 (Volca-Motion) and PID2022-140483NB-C21 (HARMONI) to AED.

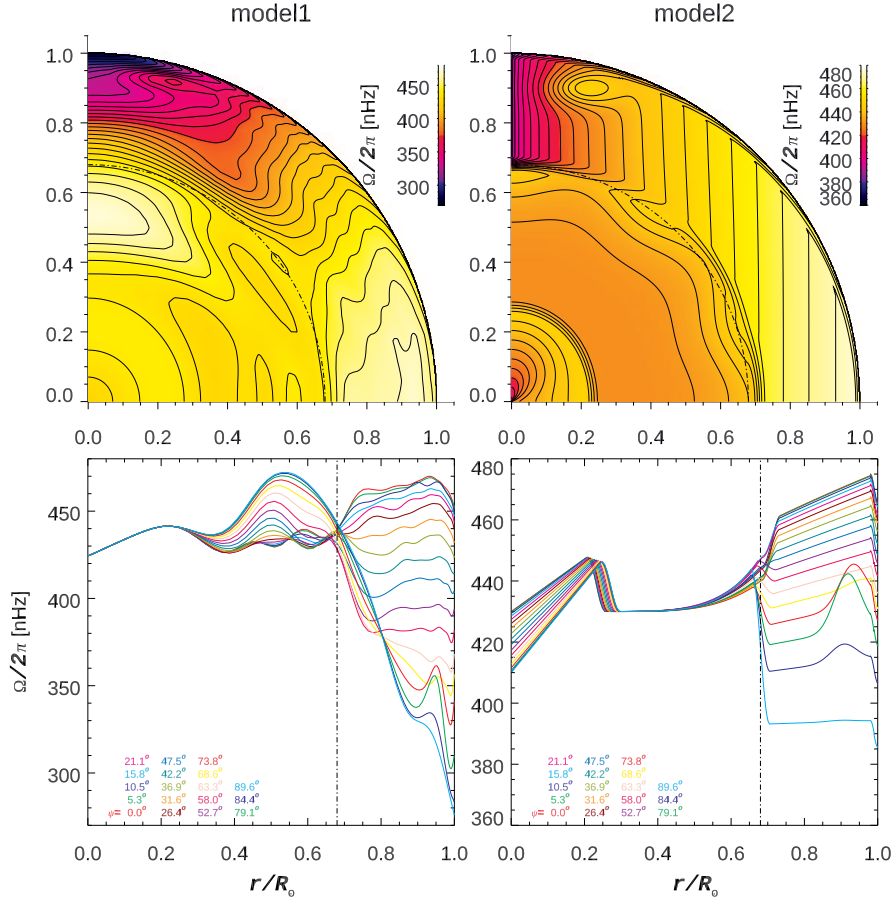


Figure 1. Speculative rotation profiles used to produce artificial rotational splittings. The two panels in the top row show them in Cartesian coordinates, while the two panels in the bottom row show cuts versus radius at selected latitudes. The two panels on the left correspond to model 1, a model that includes a feature at high latitudes, a quasi-periodic modulation in the convection zone and a wide tachocline, while the two panels on the right correspond to model 2, a model that includes a high latitude “jet”, a narrow tachocline with some modulation with latitude and a “feature” in the inner 30% radius. In both cases a near-surface shear layer was included.

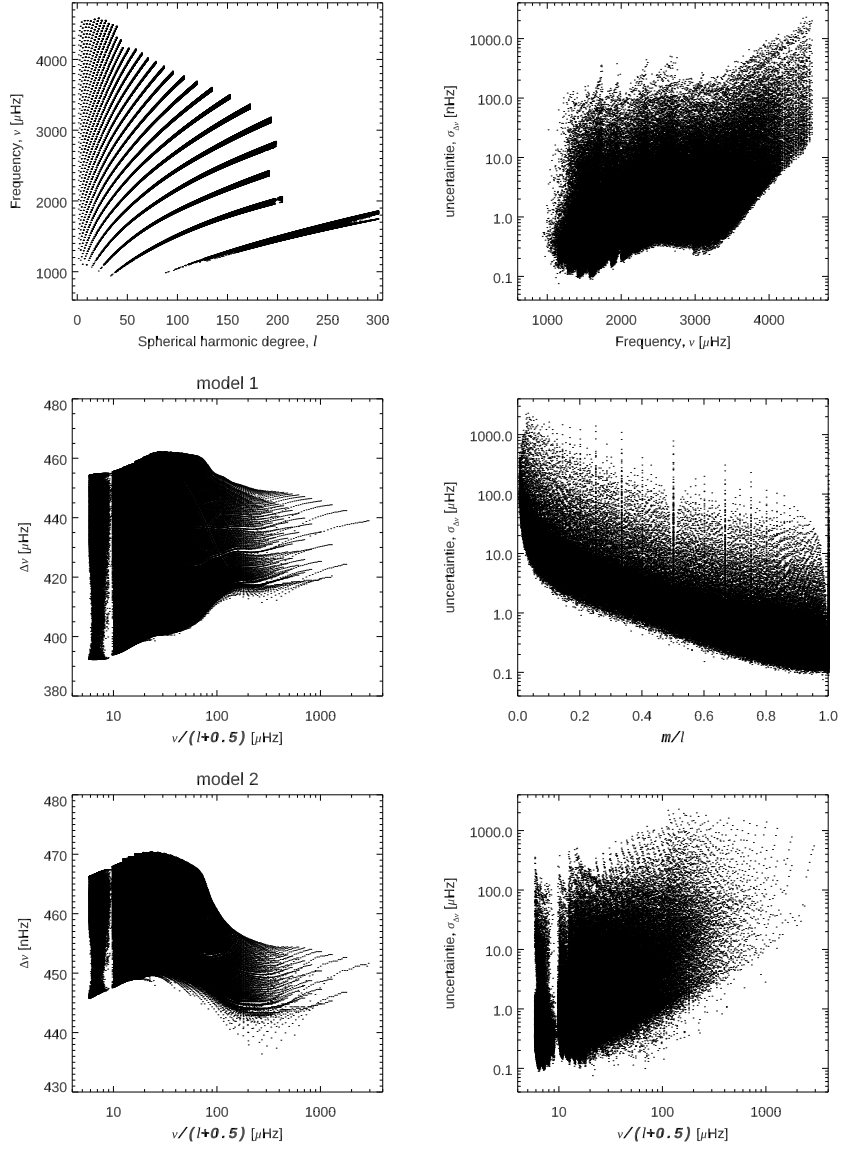


Figure 2. Artificial data sets: the upper left panel shows the coverage of the data set in the ℓ - ν space, while the middle left and bottom left panels show the rotational splittings for model 1 and model 2 respectively, as a function of $\nu/(\ell + 0.5)$, a proxy for the inner turning points of the modes. The panels on the right show the uncertainties plotted versus the mode frequency, the m/ℓ ratio and $\nu/(\ell + 0.5)$, in the top to bottom panels, respectively.

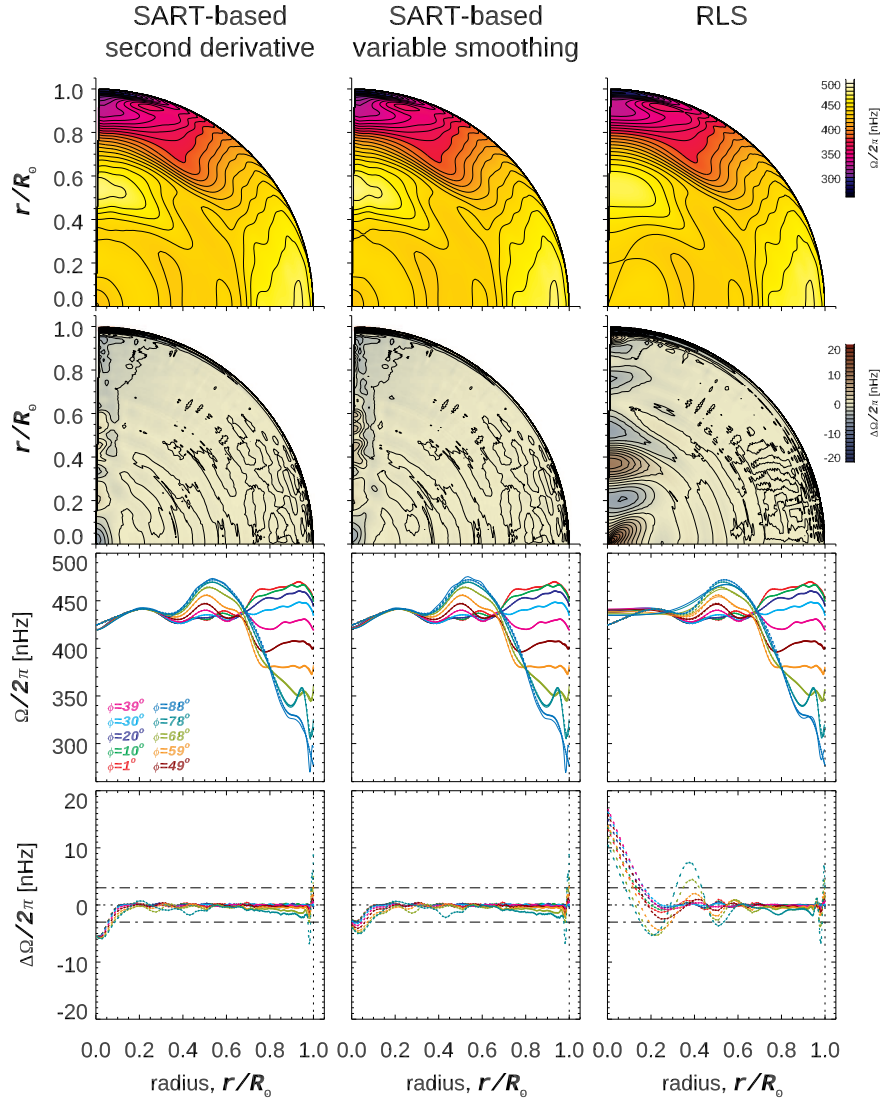


Figure 3. Inverted solutions, based on noiseless artificial splittings, corresponding to model 1. The panels show the inferred solution and the difference between that inferred solution and the actual rotation model, in Cartesian coordinates in the top two rows or as cuts versus radius at a set of latitudes in the bottom two rows. The panels in the left column correspond to the SART-based inversion using a second derivative smoothing, the panels in the middle column correspond to the SART-based inversion using a variable smoothing used for regularization, while the panels in the rightmost column show the solution when using a conventional RLS inversion methodology.

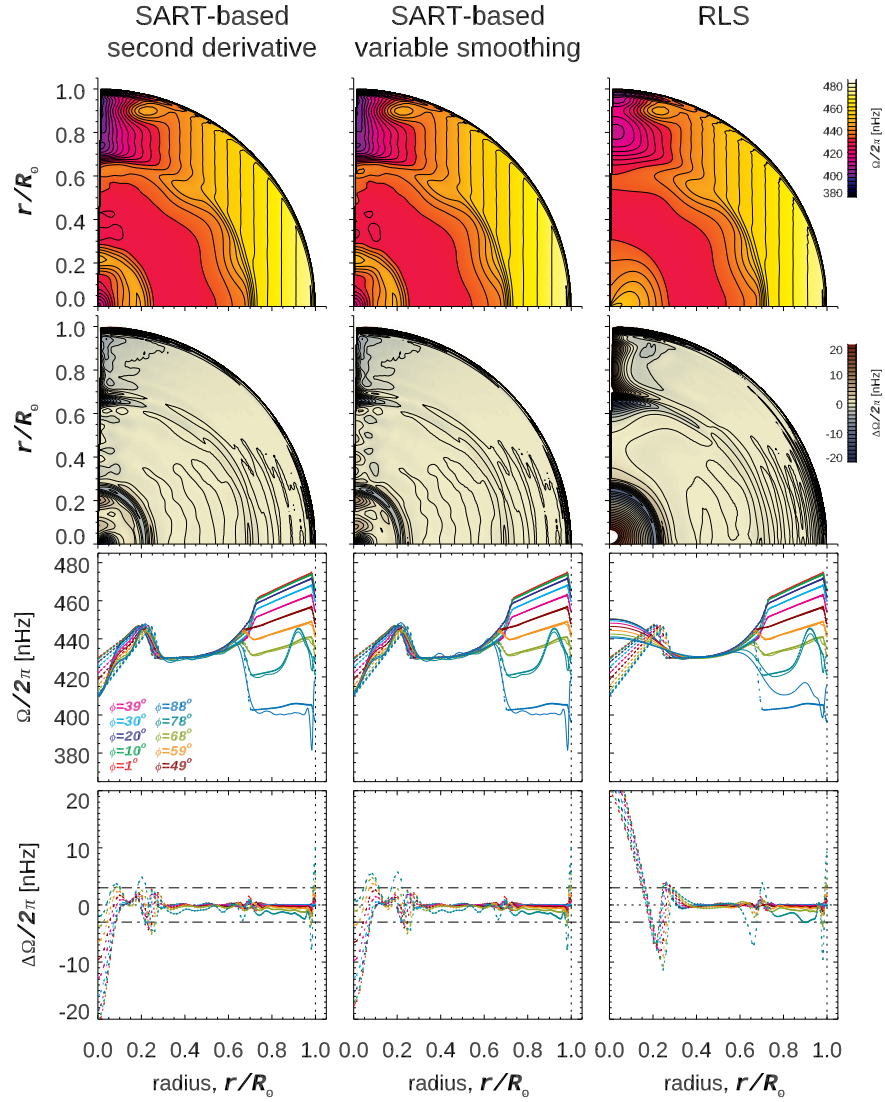


Figure 4. Inverted solution, based on noiseless artificial splittings, corresponding to model 2. The panels show the inferred solution and the difference between that inferred solution and the actual rotation model, in Cartesian coordinates in the top two rows or as cuts versus radius at a set of latitudes in the bottom two rows. The panels in the left column correspond to the SART-based inversion using a second derivative smoothing, the panels in the middle column correspond to the SART-based inversion using a variable smoothing used for regularization, while the panels in the rightmost column show the solution when using a conventional RLS inversion methodology.

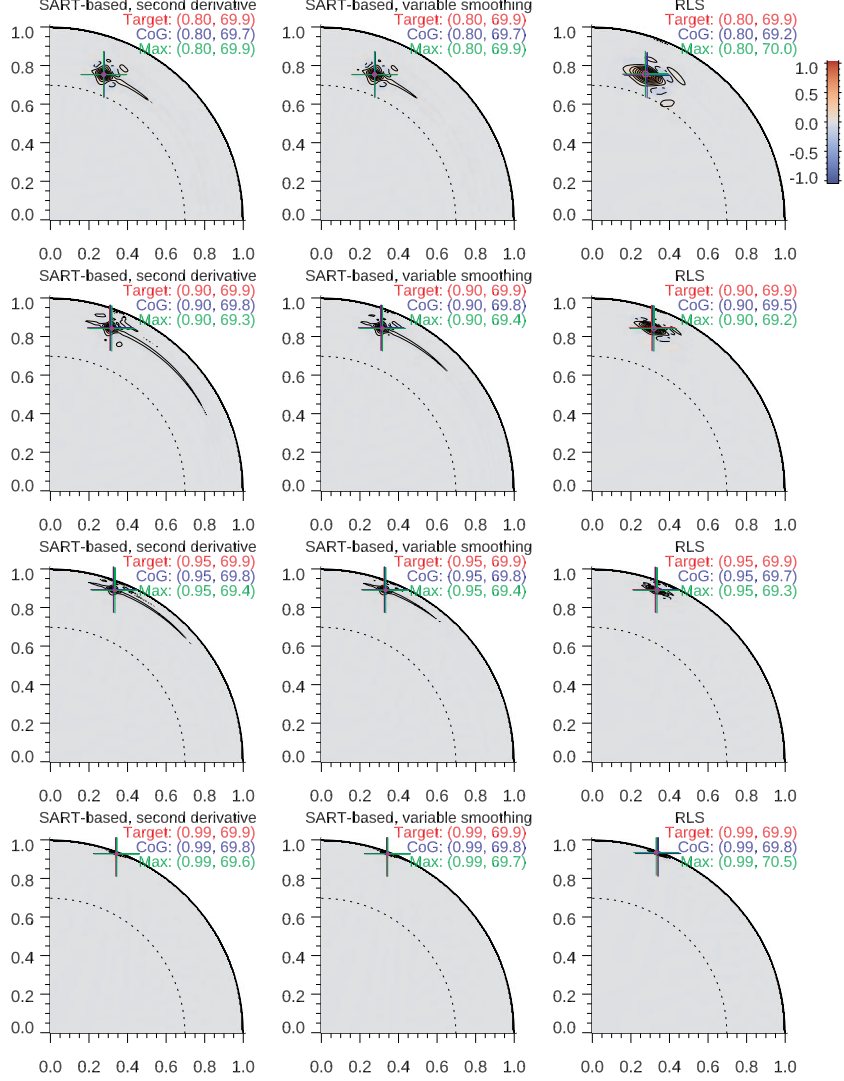


Figure 5. Averaging kernels for solutions shown in Figures 3 and 4, when using noiseless artificial splittings. The panels in each row show them at various depths near the surface ($r/R_{\odot} = 0.8, 0.9, 0.95, 0.99$) at a high target latitude, namely $\phi = 70^{\circ}$. The panels on the left correspond to the SART-based method when using a second derivative smoothing, the panels in the middle to the SART-based method when using a variable smoothing for regularization, while the panels on the right correspond to using a RLS inversion methodology. The position of the target location, the center of gravity, and the maximum of the kernels are color coded, marked as crosses and labeled as (r, ϕ) .

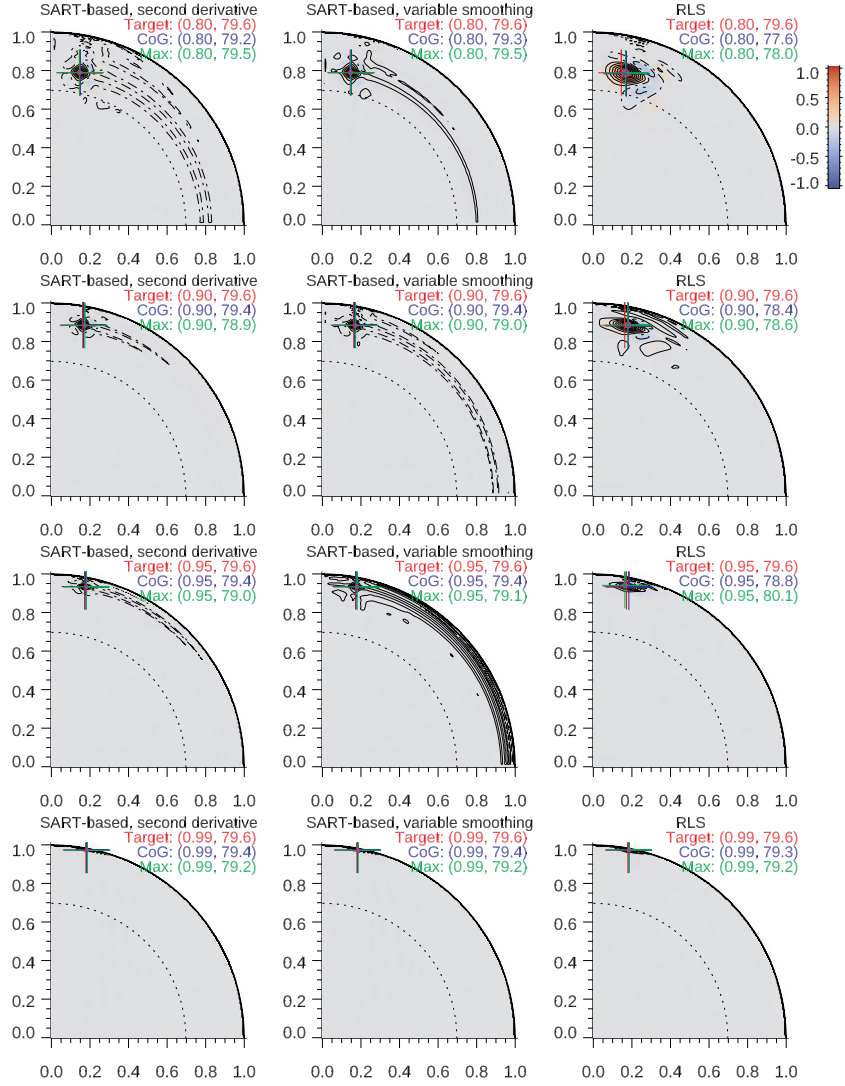


Figure 6. Averaging kernels for solutions shown in Figures 3 and 4, when using noiseless artificial splittings. The panels in each row show them at various depths near the surface ($r/R_\odot = 0.8, 0.9, 0.95, 0.99$) at an even higher target latitude, namely $\phi = 80^\circ$. The panels on the left correspond to the SART-based method when using a second derivative smoothing, the panels in the middle to the SART-based method when using a variable smoothing for regularization, while the panels on the right correspond to using a RLS inversion methodology. The position of the target location, the center of gravity, and the maximum of the kernels are color coded, marked as crosses and labeled as (r, ϕ) .

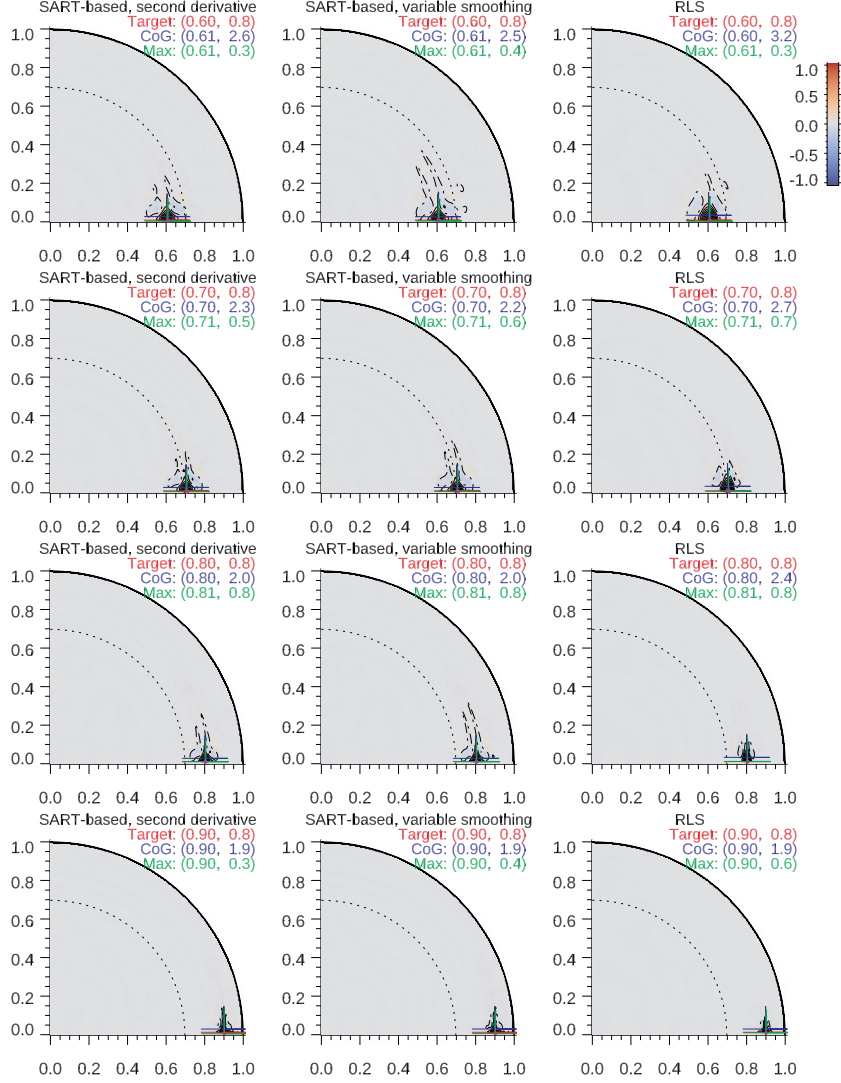


Figure 7. Averaging kernels for solutions shown in Figures 3 and 4, when using noiseless artificial splittings. The panels in each row show them at various depths ($r/R_{\odot} = 0.6, 0.7, 0.8, 0.9$) at the equatorial target latitude, namely $\phi = 0^\circ$. The panels on the top row correspond to the SART-based method when using a second derivative smoothing, the panels in the middle row to the SART-based method when using a variable smoothing for regularization, while the panels in the bottom row correspond to using a RLS inversion methodology. The position of the target location, the center of gravity, and the maximum of the kernels are color coded, marked as crosses and labeled as (r, ϕ) .

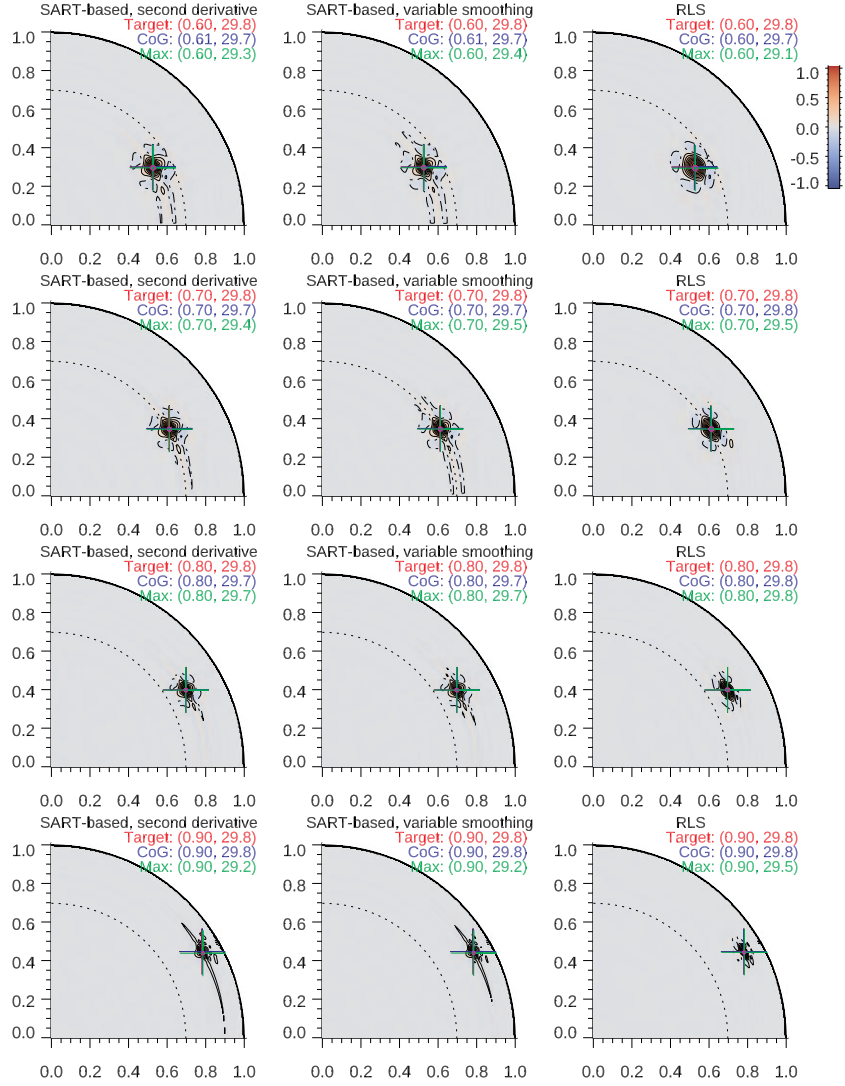


Figure 8. Averaging kernels for solutions shown in Figures 3 and 4, when using noiseless artificial splittings. The panels in each row show them at various depths in the outer 40% ($r/R_{\odot} = 0.6, 0.7, 0.8, 0.9$) at a low target latitude, namely $\phi = 30^{\circ}$. The panels on the left correspond to the SART-based method when using a second derivative smoothing, the panels in the middle to the SART-based method when using a variable smoothing for regularization, while the panels on the right correspond to using a RLS inversion methodology. The position of the target location, the center of gravity, and the maximum of the kernels are color coded, marked as crosses and labeled as (r, ϕ) .

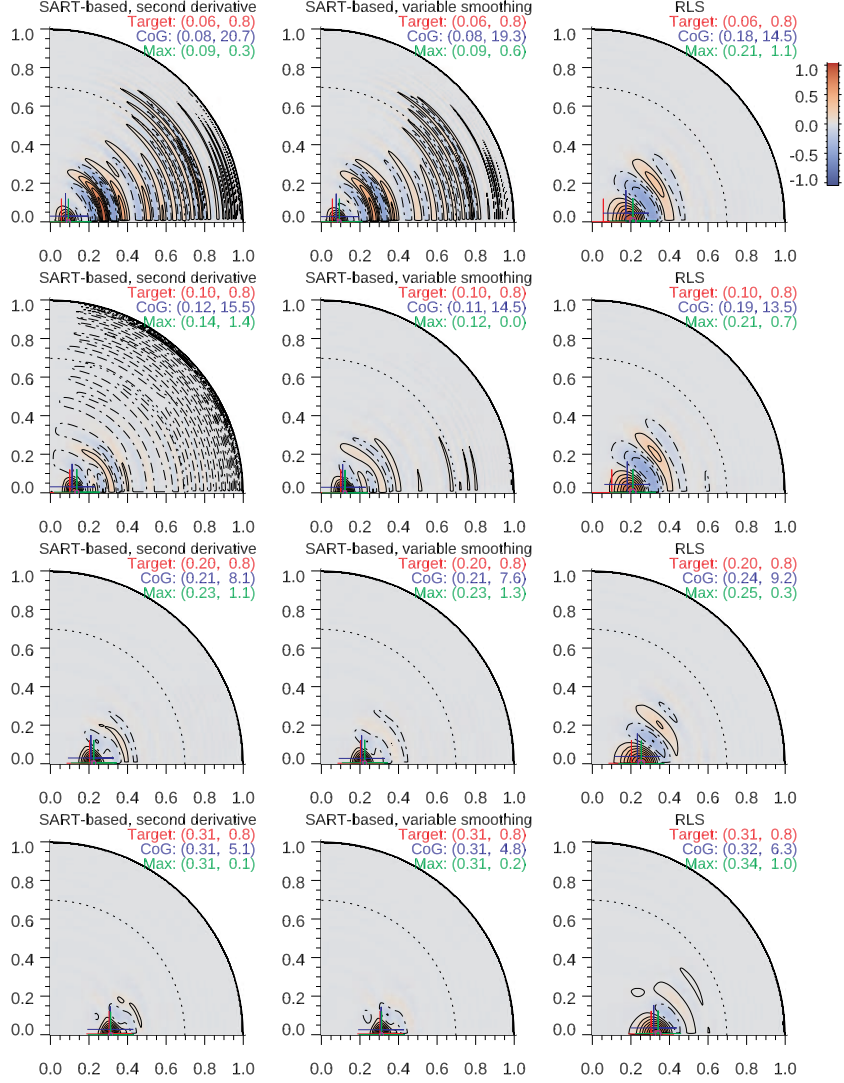


Figure 9. Averaging kernels for solutions shown in Figures 3 and 4, when using noiseless artificial splittings. The panels in each row show them at various depths in the inner 30% ($r/R_\odot = 0.06, 0.1, 0.2, 0.3$) at the equatorial target latitude, namely $\phi = 0$. The panels on the left correspond to the SART-based method when using a second derivative smoothing, the panels in the middle to the SART-based method when using a variable smoothing for regularization, while the panels on the right correspond to using a RLS inversion methodology. The position of the target location, the center of gravity, and the maximum of the kernels are color coded, marked as crosses and labeled as (r, ϕ) .

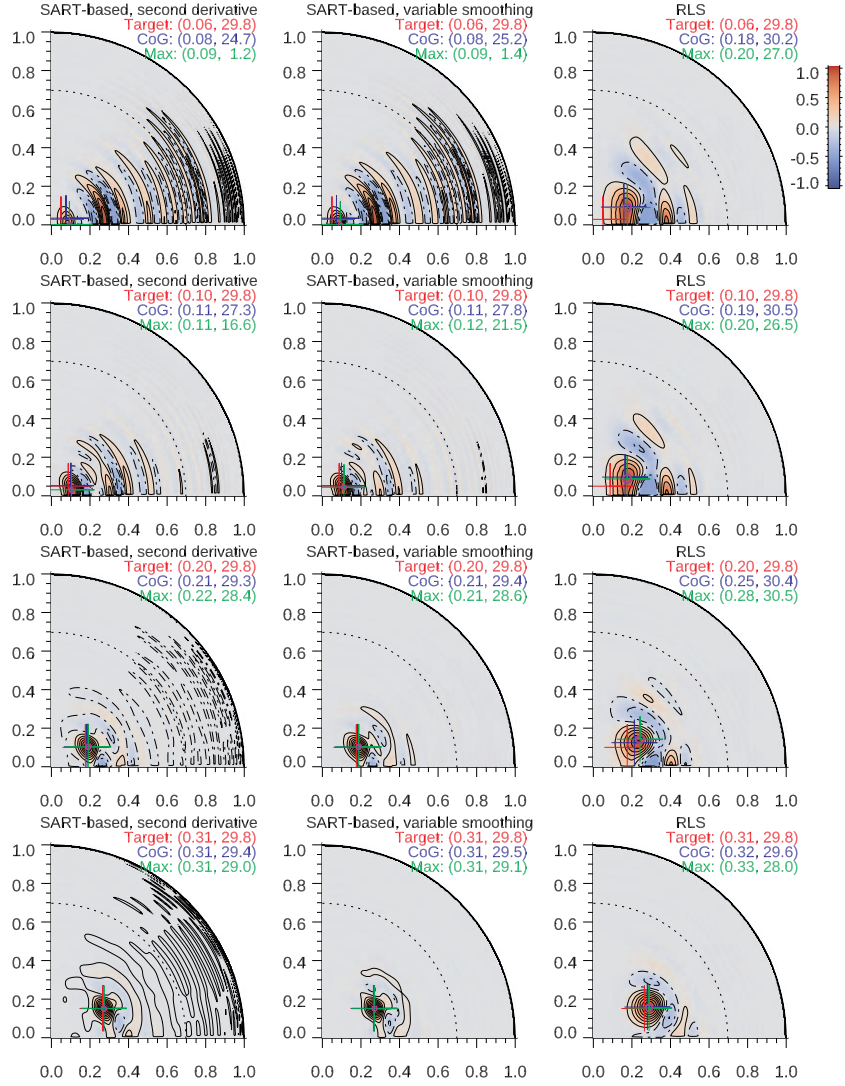


Figure 10. Averaging kernels for solutions shown in Figures 3 and 4, when using noiseless artificial splittings. The panels in each row show them at various depths in the inner 30% ($r/R_\odot = 0.06, 0.1, 0.2, 0.3$) at a low target latitudes, namely $\phi = 30^\circ$. The panels on the left correspond to the SART-based method when using a second derivative smoothing, the panels in the middle to the SART-based method when using a variable smoothing for regularization, while the panels on the right correspond to using a RLS inversion methodology. The position of the target location, the center of gravity, and the maximum of the kernels are color coded, marked as crosses and labeled as (r, ϕ) .

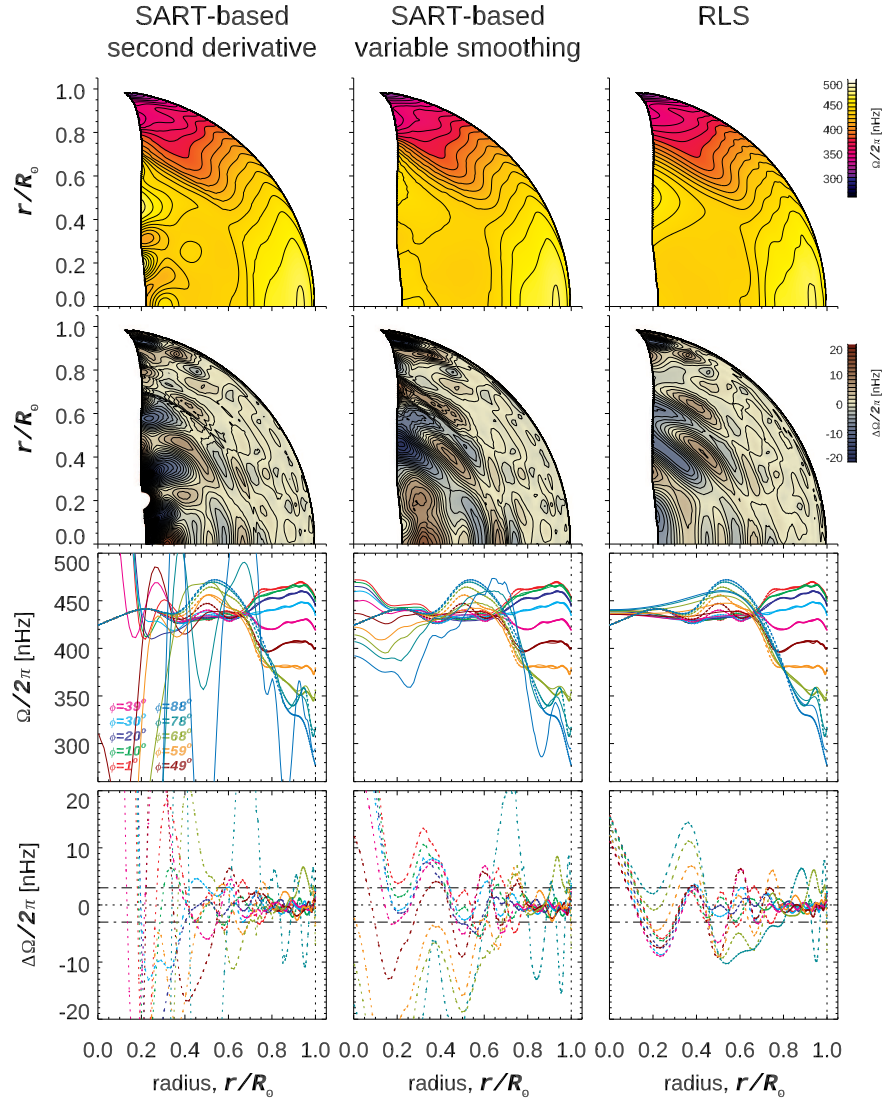


Figure 11. Inverted solution, based on artificial splittings with random noise, corresponding to model 1. The panels show the inferred solution and the difference between that inferred solution and the actual rotation model, in Cartesian coordinates in the top two rows or as cuts versus radius at a set of latitudes in the bottom two rows. The panels in the left column correspond to the SART-based inversion using a second derivative smoothing, the panels in the middle column correspond to the SART-based inversion using a variable smoothing used for regularization, while the panels in the rightmost column show the solution when using a conventional RLS inversion methodology.

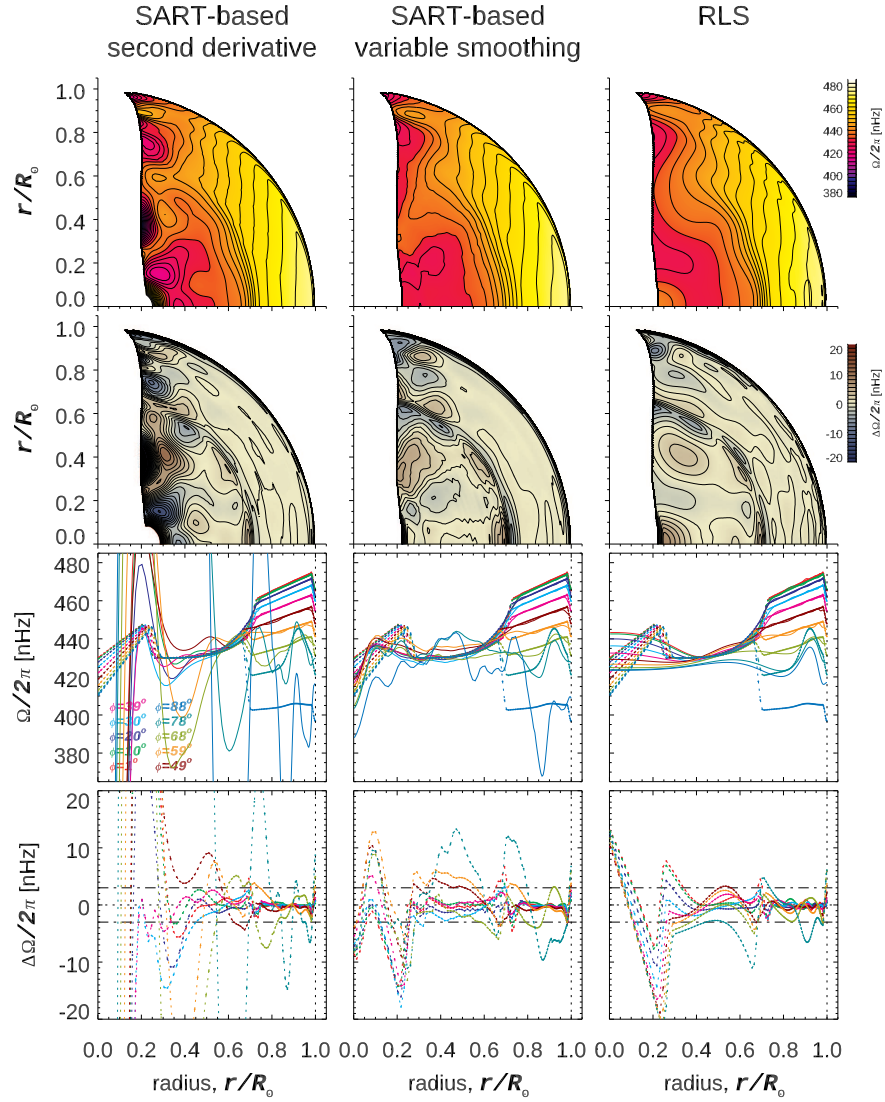


Figure 12. Inverted solution, based on artificial splittings with random noise, corresponding to model 2. The panels show the inferred solution and the difference between that inferred solution and the actual rotation model, in Cartesian coordinates in the top two rows or as cuts versus radius at a set of latitudes in the bottom two rows. The panels in the left column correspond to the SART-based inversion using a second derivative smoothing, the panels in the middle column correspond to the SART-based inversion using a variable smoothing used for regularization, while the panels in the rightmost column show the solution when using a conventional RLS inversion methodology.

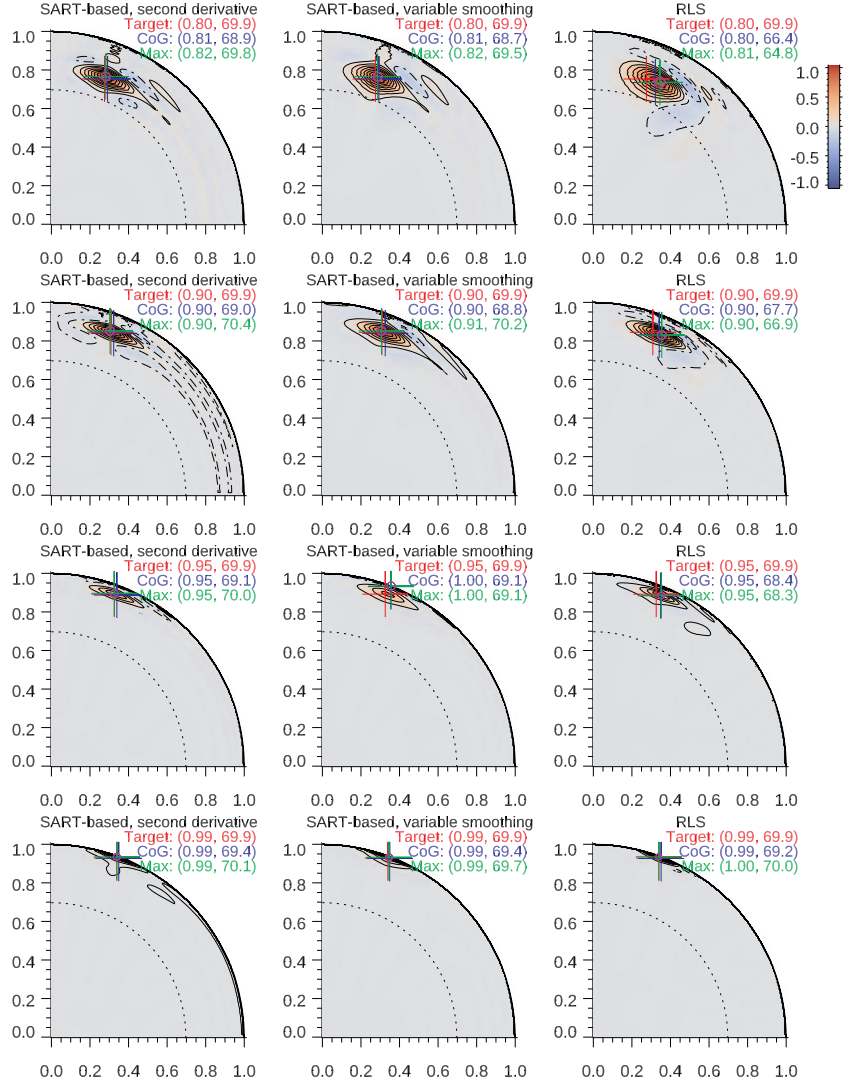


Figure 13. Averaging kernels for solutions shown in Figures 11 and 12, when using artificial splittings with random noise. Remember that in the presence of noise, for all other things equal, the averaging kernels become wider since the regularization had to be increased to limit the noise magnification. The panels in each row show them at various depths near the surface ($r/R_\odot = 0.8, 0.9, 0.95, 0.99$) at a high target latitude, namely $\phi = 70^\circ$. The panels on the left correspond to the SART-based method when using a second derivative smoothing, the panels in the middle to the SART-based method when using a variable smoothing for regularization, while the panels on the right correspond to using a RLS inversion methodology. The position of the target location, the center of gravity, and the maximum of the kernels are color coded, marked as crosses and labeled as (r, ϕ) .

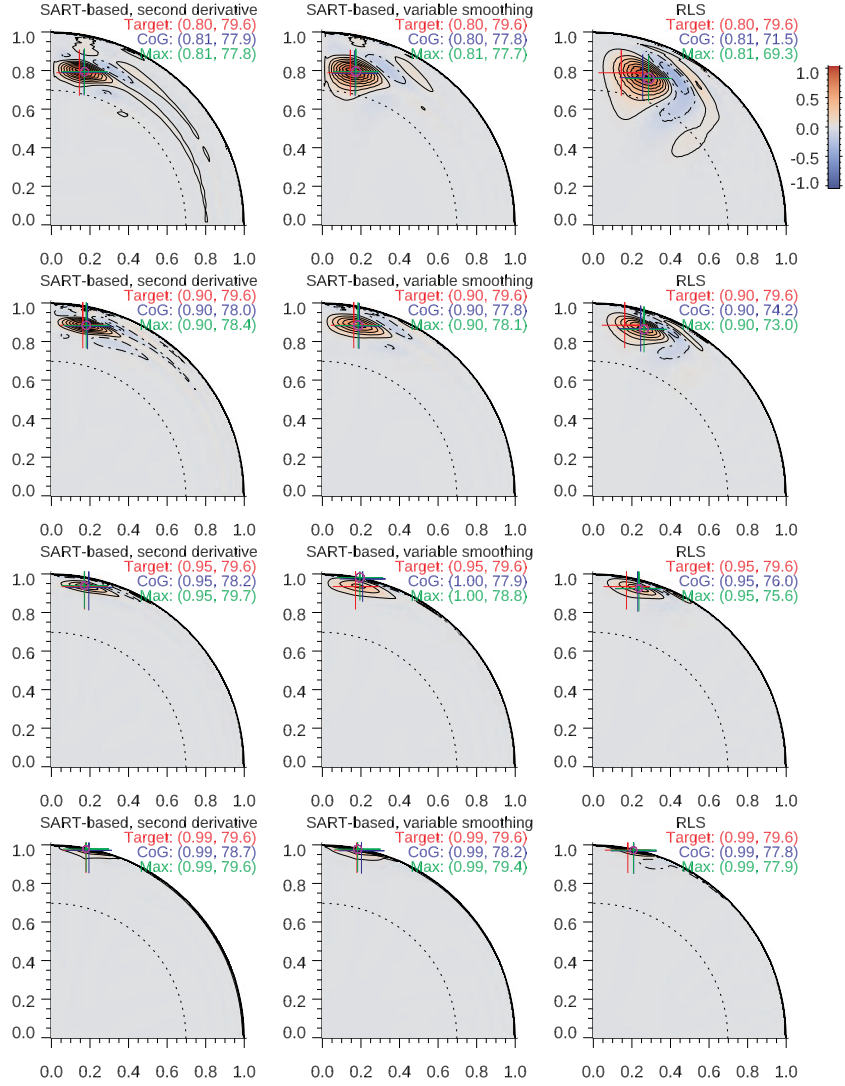


Figure 14. Averaging kernels for solutions shown in Figures 11 and 12, when using artificial splittings with random noise. The panels in each row show them at various depths near the surface ($r/R_\odot = 0.8, 0.9, 0.95, 0.99$) at an even higher target latitude, namely $\phi = 80^\circ$. The panels on the left correspond to the SART-based method when using a second derivative smoothing, the panels in the middle to the SART-based method when using a variable smoothing for regularization, while the panels on the right correspond to using a RLS inversion methodology. The position of the target location, the center of gravity, and the maximum of the kernels are color coded, marked as crosses and labeled as (r, ϕ) .

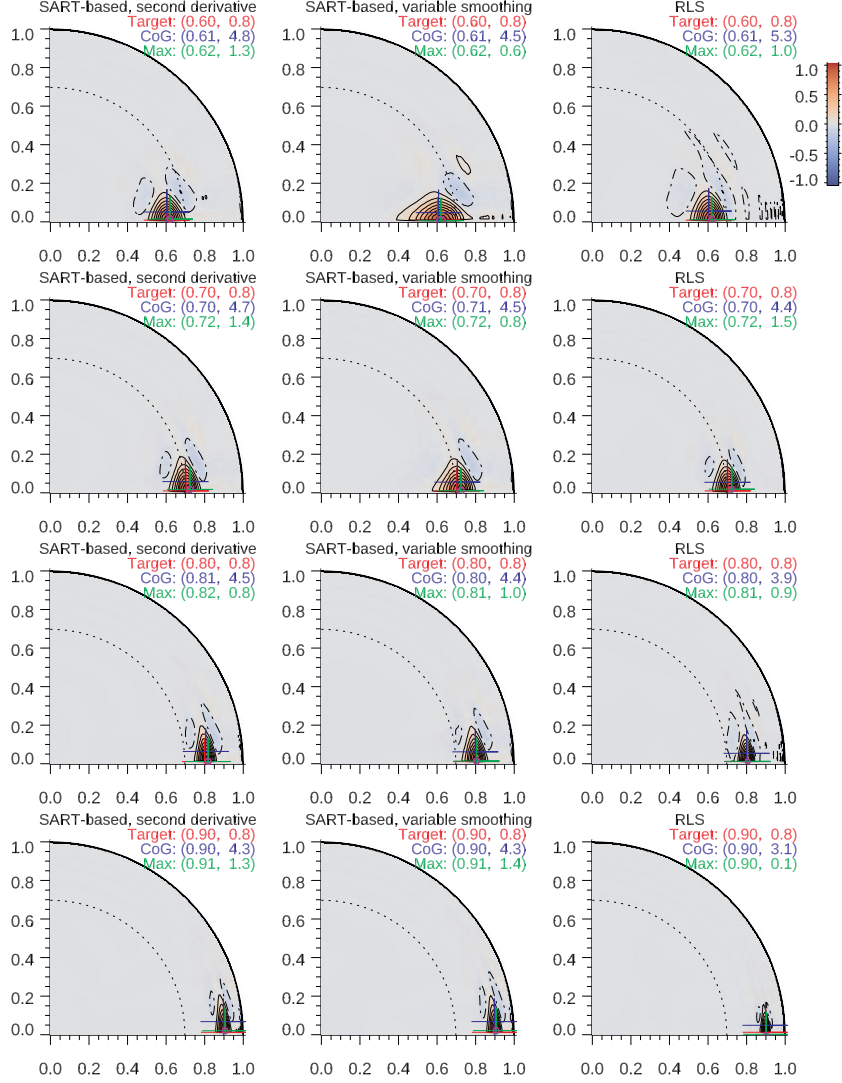


Figure 15. Averaging kernels for solutions shown in Figures 11 and 12, when using artificial splittings with random noise. The panels in each row show them at various depths in the outer 40% ($r/R_{\odot} = 0.6, 0.7, 0.8, 0.9$) at the equatorial target latitude, namely $\phi = 0^{\circ}$. The panels on the left correspond to the SART-based method when using a second derivative smoothing, the panels in the middle to the SART-based method when using a variable smoothing for regularization, while the panels on the right correspond to using a RLS inversion methodology. The position of the target location, the center of gravity, and the maximum of the kernels are color coded, marked as crosses and labeled as (r, ϕ) .

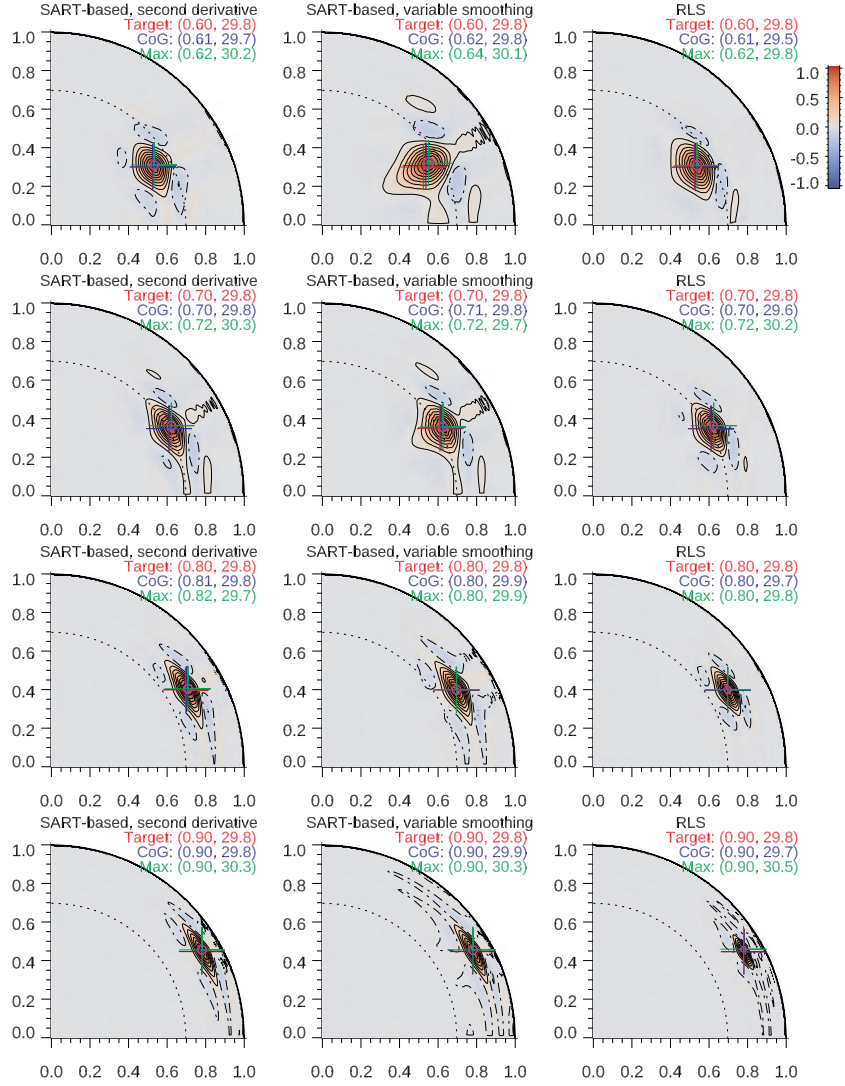


Figure 16. Averaging kernels for solutions shown in Figures 11 and 12, when using artificial splittings with random noise. The panels in each row show them at various depths in the outer 40% ($r/R_{\odot} = 0.6, 0.7, 0.8, 0.9$) at a low target latitude, namely $\phi = 30^{\circ}$. The panels on the left correspond to the SART-based method when using a second derivative smoothing, the panels in the middle to the SART-based method when using a variable smoothing for regularization, while the panels on the right correspond to using a RLS inversion methodology. The position of the target location, the center of gravity, and the maximum of the kernels are color coded, marked as crosses and labeled as (r, ϕ) .

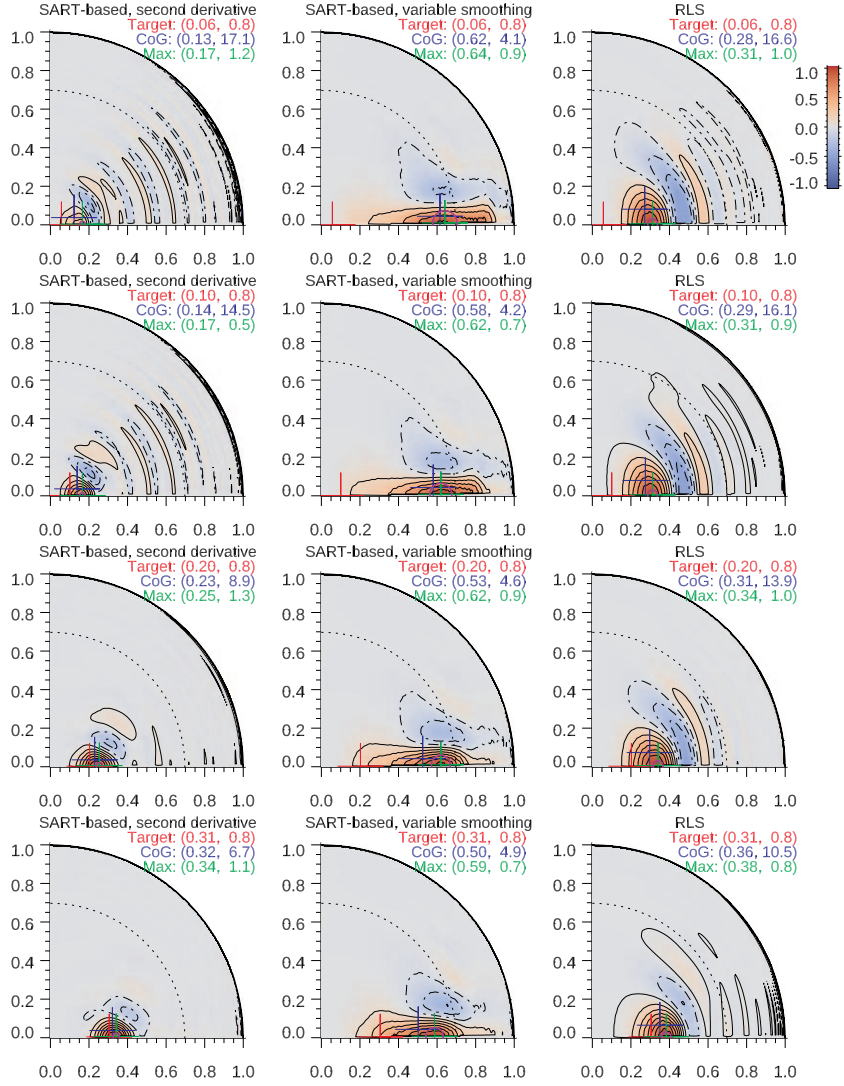


Figure 17. Averaging kernels for solutions shown in Figures 11 and 12, when using artificial splittings with random noise. The panels in each row show them at various depths in the inner 30% ($r/R_\odot = 0.06, 0.1, 0.2, 0.3$) at the equatorial target latitude, namely $\phi = 0^\circ$. The panels on the left correspond to the SART-based method when using a second derivative smoothing, the panels in the middle to the SART-based method when using a variable smoothing for regularization, while the panels on the right correspond to using a RLS inversion methodology. The position of the target location, the center of gravity, and the maximum of the kernels are color coded, marked as crosses and labeled as (r, ϕ) .

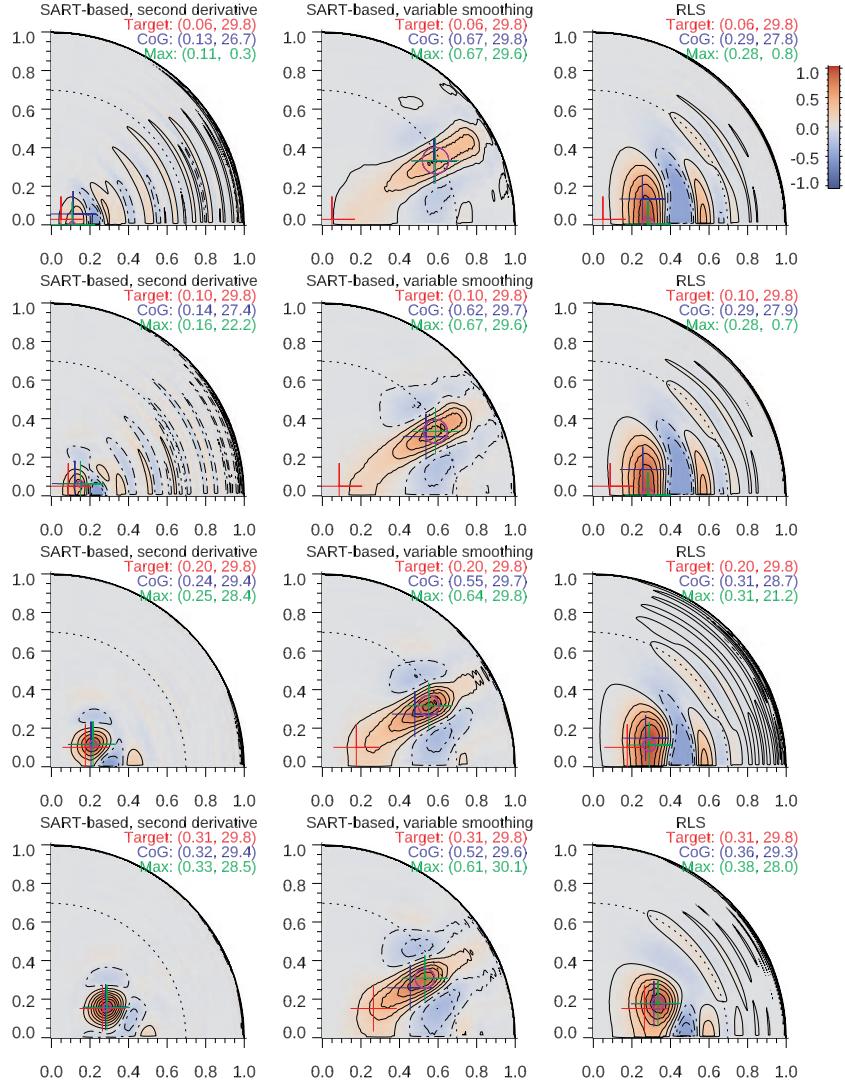


Figure 18. Averaging kernels for solutions shown in Figures 11 and 12, when using artificial splittings with random noise. The panels in each row show them at various depths in inner 30% ($r/R_{\odot} = 0.06, 0.1, 0.2, 0.3$) at a low target latitude, namely $\phi = 30^{\circ}$. The panels on the left correspond to the SART-based method when using a second derivative smoothing, the panels in the middle to the SART-based method when using a variable smoothing for regularization, while the panels on the right correspond to using a RLS inversion methodology. The position of the target location, the center of gravity, and the maximum of the kernels are color coded, marked as crosses and labeled as (r, ϕ) .

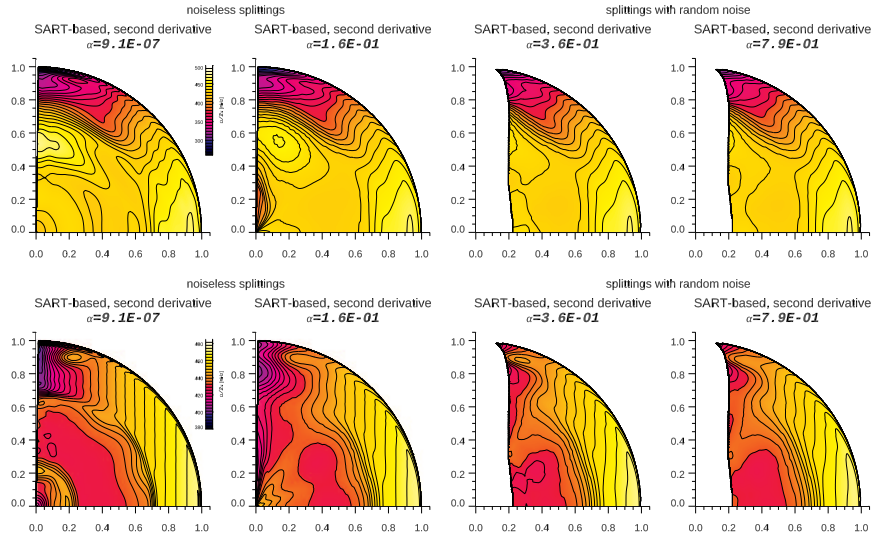


Figure 19. Effect of adjusting the regularization factor, α , when using the SART-based inversion methodology and the variable smoothing for regularization for either model (top and bottom panels), for both noiseless and noisy splittings for two values of α (left to right panels).

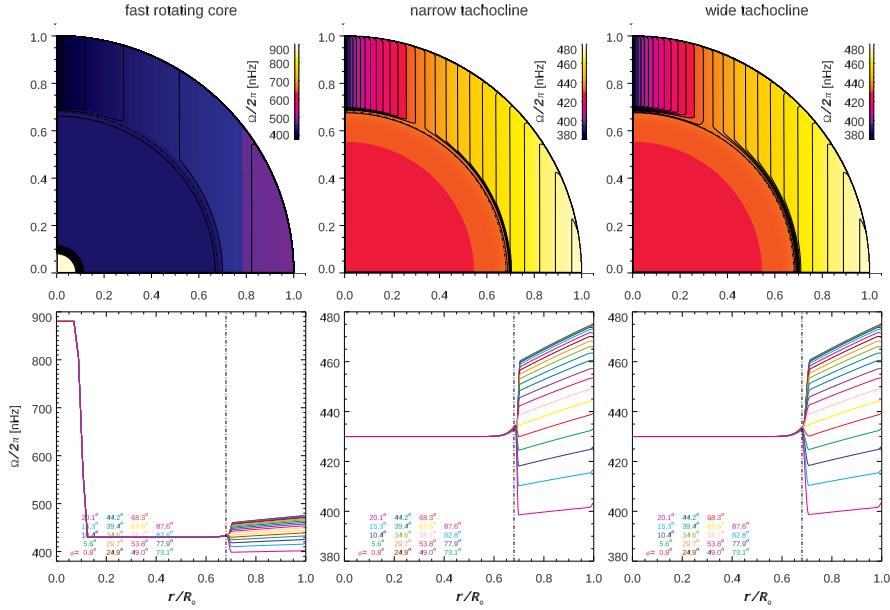


Figure 20. Additional rotation models used to compute artificial splittings. From left to right: models with (i) a rapidly rotating core, (ii) a narrow tachocline, and (iii) a wider tachocline. The top panels show them in Cartesian coordinates, while the bottom panels show cuts versus radius at selected latitudes.

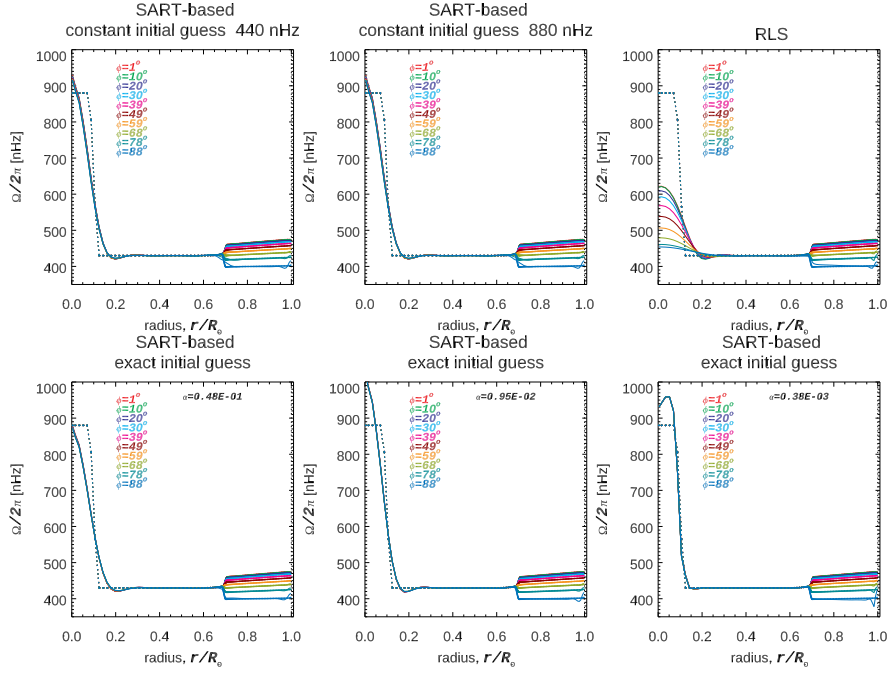


Figure 21. Inverted profiles when using artificial noiseless splittings corresponding to a rapidly rotating core. The solution for the RLS inversion (upper right panel) is compared to the SART-based inversion using the second derivative smoothing, a constant initial guess for two different values (upper left and middle panels), and an initial guess that is the known underlying profile for three different regularization values (lower panels).

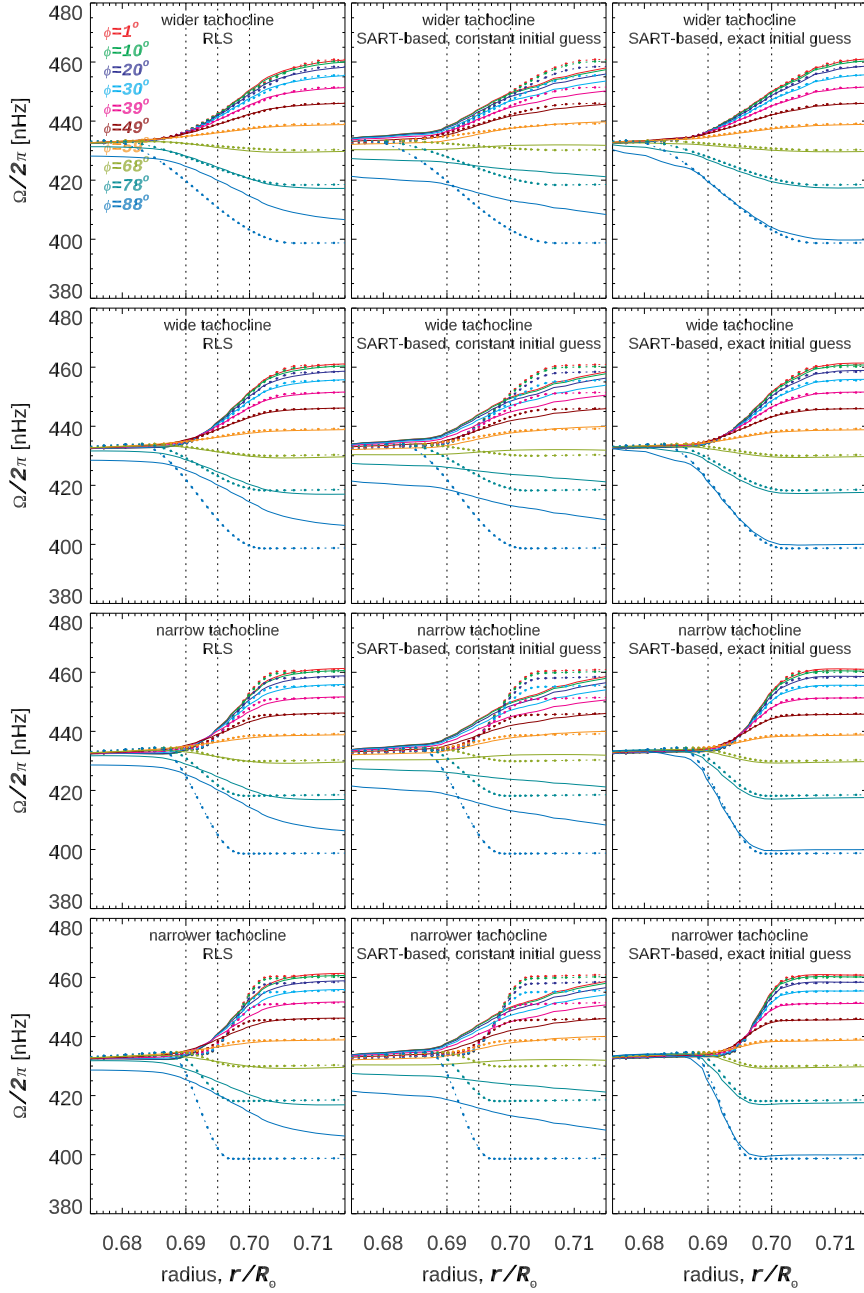


Figure 22. Inverted profiles when using artificial noiseless splittings corresponding to four different thicknesses of the tachocline (top to bottom panels). The solution for the RLS inversion is compared to the SART-based inversion using a constant initial guess and an initial guess that is the known underlying profile (left to right panels). Fiducial lines are added only to guide the eye since only a small fraction of the radial range is shown.

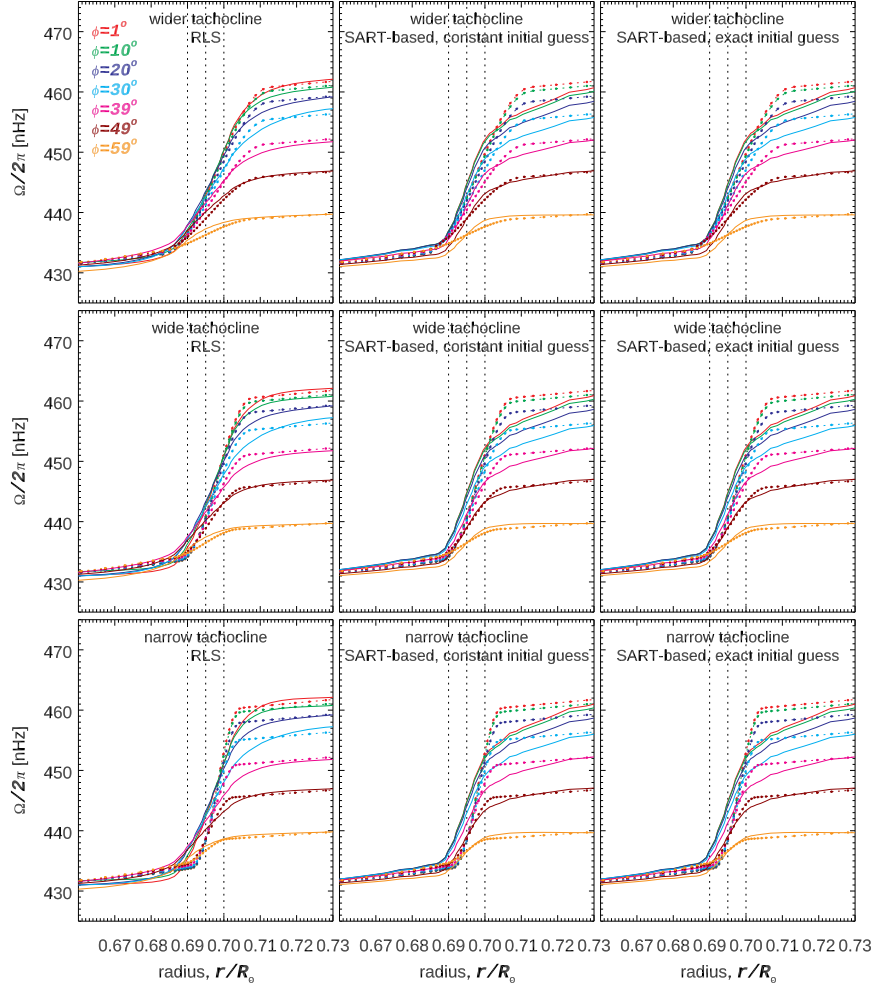


Figure 23. Inverted profiles when using artificial splittings with little random noise corresponding to three different thicknesses of the tachocline (top to bottom panels). the solution for the RLS inversion is compared to the SART-based inversion using a constant initial guess and an initial guess that is the known underlying profile (left to right panels). Fiducial lines are added only to guide the eye since only a small fraction of the radial range is shown and for a limited range in latitudes.

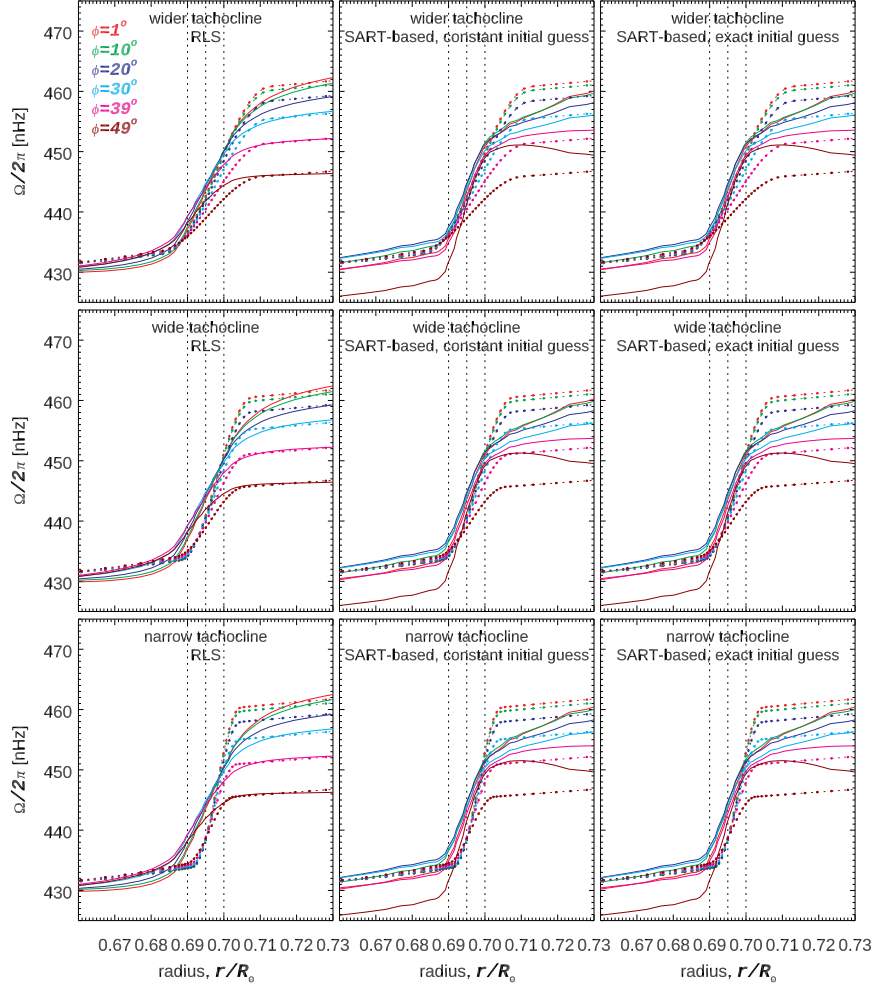


Figure 24. Inverted profiles when using artificial splittings with random noise corresponding to three different thicknesses of the tachocline (top to bottom panels). The solution for the RLS inversion is compared to the SART-based inversion using a constant initial guess and an initial guess that is the known underlying profile (left to right panels). This figure shows that the more narrow tachocline models are not well recovered in all cases, but also how the SART-based inferences present other systematic errors near the tachocline at higher latitudes. Fiducial lines are added only to guide the eye since only a small fraction of the radial range is shown and for a limited range in latitudes.

Table 1. RMS of the differences with respect to the input model profile for cuts at various latitudes when inverting noiseless artificial splittings.

r/R_{\odot}	SART-based second derivative				SART-based variable smoothing				RLS			
	[0-0.3]	[0.3-0.7]	[0.7-1]	[0-1]	[0-0.3]	[0.3-0.7]	[0.7-1]	[0-1]	[0-0.3]	[0.3-0.7]	[0.7-1]	[0-1]
lat.	model 1											
0.8	2.3	0.2	0.1	1.0	1.2	0.2	0.1	0.5	6.0	0.5	0.1	2.6
10.5	2.3	0.1	0.1	1.0	1.2	0.1	0.2	0.5	6.2	0.3	0.1	2.7
20.1	2.4	0.1	0.1	1.0	1.3	0.1	0.1	0.6	7.1	0.3	0.1	3.0
29.8	2.4	0.1	0.2	1.0	1.4	0.1	0.2	0.6	8.0	0.2	0.2	3.4
39.4	2.5	0.2	0.2	1.1	1.7	0.2	0.2	0.7	8.2	0.3	0.2	3.5
49.0	2.6	0.2	0.5	1.2	2.0	0.2	0.5	0.9	7.6	0.7	0.5	3.3
58.7	2.8	0.4	0.8	1.3	2.3	0.3	0.9	1.2	6.6	1.1	0.8	2.9
68.3	2.9	0.4	1.5	1.7	2.6	0.4	1.4	1.5	5.7	2.0	1.4	2.9
78.0	3.0	0.8	2.6	2.3	2.6	0.9	2.6	2.3	5.0	3.4	2.3	3.3
lat.	model 2											
0.8	8.3	0.4	0.2	3.5	7.1	0.3	0.2	3.0	10.4	0.3	0.2	4.4
10.5	8.1	0.2	0.1	3.4	6.8	0.2	0.1	2.9	10.8	0.3	0.2	4.6
20.1	7.4	0.2	0.1	3.1	6.1	0.2	0.1	2.6	11.5	0.2	0.1	4.9
29.8	6.3	0.2	0.2	2.7	5.1	0.2	0.1	2.2	12.5	0.3	0.2	5.3
39.4	5.1	0.2	0.3	2.2	3.9	0.2	0.3	1.7	13.5	0.3	0.3	5.7
49.0	3.9	0.3	0.5	1.7	2.9	0.3	0.5	1.3	14.3	0.4	0.5	6.1
58.7	2.9	0.4	0.8	1.4	2.4	0.4	0.9	1.2	14.8	0.7	0.8	6.3
68.3	2.4	0.5	1.5	1.5	2.6	0.5	1.5	1.6	15.1	0.8	1.5	6.5
78.0	2.7	1.1	3.0	2.5	3.4	1.0	3.0	2.7	15.3	2.3	3.5	7.1

Table 2. RMS of the differences with respect to the input model profile for cuts at various latitudes when inverting artificial splittings with random noise.

r/R_{\odot}	SART-based second derivative				SART-based variable smoothing				RLS			
	[0-0.3]	[0.3-0.7]	[0.7-1]	[0-1]	[0-0.3]	[0.3-0.7]	[0.7-1]	[0-1]	[0-0.3]	[0.3-0.7]	[0.7-1]	[0-1]
lat.	model 1											
0.8	483.1	6.9	1.1	205.6	26.1	6.3	1.5	11.7	7.7	2.1	1.1	3.6
10.5	474.8	2.8	1.1	202.0	24.0	4.8	1.4	10.6	7.6	1.5	0.7	3.4
20.1	431.6	5.5	0.9	183.7	21.2	3.8	0.9	9.3	7.3	1.4	0.7	3.2
29.8	315.8	4.7	1.0	134.4	18.5	4.4	1.1	8.2	7.1	2.1	0.8	3.3
39.4	127.0	6.5	0.8	54.1	12.5	5.0	1.1	6.0	6.9	3.7	0.7	3.6
49.0	138.4	10.8	1.1	59.2	8.3	4.5	1.6	4.4	6.2	4.4	1.2	3.6
58.7	354.4	9.3	1.7	150.9	19.1	8.2	2.2	9.3	5.6	4.9	2.0	3.8
68.3	544.6	21.1	3.2	232.0	29.2	11.5	4.1	14.2	6.4	7.4	3.0	5.3
78.0	703.0	61.6	10.4	301.0	40.8	14.9	10.2	20.5	7.9	9.3	5.1	7.1
lat.	model 2											
0.8	599.2	2.9	0.7	255.0	7.5	2.0	1.3	3.5	7.0	1.9	0.8	3.2
10.5	600.1	1.8	0.5	255.3	7.2	1.0	0.9	3.2	6.9	1.3	0.6	3.0
20.1	609.9	4.3	0.4	259.5	7.4	1.0	0.8	3.3	6.7	0.8	0.4	2.9
29.8	620.4	5.9	0.4	264.0	8.0	2.0	0.8	3.6	7.4	1.2	0.6	3.3
39.4	608.7	1.7	0.6	259.0	6.5	1.0	1.0	2.9	8.7	1.3	0.7	3.8
49.0	557.6	6.1	0.9	237.3	6.2	2.9	1.3	3.2	9.7	2.1	0.8	4.3
58.7	484.6	14.3	1.7	206.3	6.5	4.0	1.8	3.7	10.6	2.2	1.4	4.8
68.3	417.9	30.1	3.4	178.5	6.8	2.9	2.6	3.8	11.3	2.5	2.0	5.2
78.0	408.3	111.4	9.4	183.7	6.2	7.2	6.9	6.9	11.8	5.4	3.6	6.3

References

- Anderson, A. H., & Kak, A. C.: 1984, *Ultrasonic Imaging* **6**, 81. doi:10.1016/0161-7346(84)90008-7
- Antia, H.M. and Basu, S.: 2011, *Astrophys. J.* **735**, L45. doi:10.1088/2041-8205/735/2/L45.
- Backus, G., and Gilbert, F.: 1968, *Geophysical Journal* **16(2)**, 169. doi:10.1111/j.1365-246X.1968.tb00216.x
- Barekat, A., Schou, J., & Gizon, L. 2014, *Astron. Astrophys.*, 570, L12. doi:10.1051/0004-6361/201424839
- Barrett, R.K.: 1994, *Ph.D. Thesis*.
- Basu, S.: 2016, *Living Reviews in Solar Physics* **13**, 2. doi:10.1007/s41116-016-0003-4
- Basu, S. and Antia, H.M.: 2019, *Astrophys. J.* **883**, 93. doi:10.3847/1538-4357/ab3b57.
- Corbard, T., Berthomieu, G., Provost, J., and Morel, P.: 1998, *Astron. Astrophys.* **330**, 1149. doi:10.48550/arXiv.astro-ph/9710319.
- Chaplin, W.J. and Basu, S.: 2008, *Sol. Phys.* **251**, 53. doi:10.1007/s11207-008-9136-5.
- Christensen-Dalsgaard, J., Hansen, P.C., and Thompson, M.J.: 1993, *Mon. Not. R. Astron. Soc.* **264**, 541. doi:10.1093/mnras/264.3.541.
- Christensen-Dalsgaard, J., Dappen, W., Ajukov, S.V., Anderson, E.R., Antia, H.M., Basu, S., and, ...: 1996, *Science* **272**, 1286. doi:10.1126/science.272.5266.1286.
- Eff-Darwich, A. & Pérez Hernández, F. 1997, *Astron. Astrophys. Suppl.*, 125, 391. doi:10.1051/aas:1997229
- Eff-Darwich, A., Korzennik, S.G., Jiménez-Reyes, S.J., and García, R.A. 2008, *Astrophys. J.* **679**, 1636. doi:10.1086/586724
- Eff-Darwich, A., Korzennik, S. G., & García, R. A. 2010, *Astronomische Nachrichten*, **331**, 890. doi:10.1002/asna.201011420
- Eff-Darwich, A. and Korzennik, S.G.: 2013, *Sol. Phys.* **287**, 43. doi:10.1007/s11207-012-0048-z.
- Engl, H.W., Hanke, M., and Neubauer, A.: 1996, *Regularization of Inverse Problems*. Kluwer, Dordrecht.
- Fossat, E., Boumier, P., Corbard, T., Provost, J., Salabert, D., Schmider, F.X., and, ...: 2017, *Astron. Astrophys.* **604**, A40. doi:10.1051/0004-6361/201730460.
- Gizon, L., Birch, A.C.: 2005, *Living Rev. Sol. Phys.* **2**, 6. <https://doi.org/10.12942/lrsp-2005-6>
- Hansen, C., Cox, J., and van Horn, H.: 1977, *Astrophys. J.*, **217**, 151.
- Howe, R., Christensen-Dalsgaard, J., Hill, F., Komm, R.W., Larsen, R.M., Schou, J., and, ...: 2000, *Science* **287**, 2456. doi:10.1126/science.287.5462.2456.
- Howe, R., Christensen-Dalsgaard, J., Hill, F., Komm, R., Schou, J., and Thompson, M.J.: 2005, *Astrophys. J.* **634**, 1405. doi:10.1086/497107.
- Howe, R. 2009, *Liv. Rev. in Solar Phys*, <http://solarphysics.livingreviews.org/Articles/lrsp-2009-1/> **6**, 1.
- Howe, R.: 2016, *Asian Journal of Physics* **25**, 311.
- Korzennik, S.G.: 1990, *Ph.D. Thesis*.
- Korzennik, S.G.: 2023, *Frontiers in Astronomy and Space Sciences* **9**, 1031313. doi:10.3389/fspas.2022.1031313.
- Mathur, S., Eff-Darwich, A., García, R.A., and Turck-Chièze, S.: 2008, *Astron. Astrophys.* **484**, 517. doi:10.1051/0004-6361:20078839.
- McGaughey, W.J., and R.P. Young.: 1990, Paper presented at the 1990 SEG Annual Meeting, San Francisco, California, September 1990.
- Pijpers, F.P., & Thompson, M.J.: 1994, *Astron. Astrophys.*, **281**, 231.
- Rhodes, E.J., Cacciani, A., Korzennik, S., Tomczyk, S., Ulrich, R.K., and Woodard, M.F.: 1990, *Astrophys. J.* **351**, 687. doi:10.1086/168507.
- Scherrer, P.H. and Gough, D.O.: 2019, *Astrophys. J.* **877**, 42. doi:10.3847/1538-4357/ab13ad.
- Schou, J., Antia, H.M., Basu, S., Bogart, R.S., Bush, R.I., Chitre, S.M., and, ...: 1998, *Astrophys. J.* **505**, 390. doi:10.1086/306146.
- Schou, J., Antia, H.M., Basu, S., Bogart, R.S., Bush, R.I., Chitre, S.M., Christensen-Dalsgaard, J., Di Mauro, M.P., Dziembowski, W.A., Eff-Darwich, A., Gough, D.O., Haber, D.A., Hoeksema, J.T., Howe, R., Korzennik, S.G., Kosovichev, A.G., Larsen, R.M., Pijpers, F.P., Scherrer, P.H., Sekii, T., Tarbell, T.D., Title, A.M., Thompson, M.J. and Toomre, J.: 2008, *Astrophys. J.*, **505**, 390.
- Sorzano, C., Vargas, J., Otón, J., de la Rosa-Trevín, J., Vilas, J., Kazemi, M., Melero, R., del Caño, L., Cuenca, J., Conesa, P., Gómez-Blanco, J., and Marabini R.: 2017, *BioMed Research International* **2017**, 1. <https://doi.org/10.1155/2017/6482567>

- Sudnik, M., and M. J. Thompson, M.J.: 2009, *ASP Conference Series: Solar-Stellar Dynamos as Revealed by Helio- and Asteroseismology* **416**, 411.
- Thompson, M.J., Toomre, J., Anderson, E., Antia, H.M., Berthomieu, G., Burtonclay, D., Chitre, S.M., Christensen-Dalsgaard, J., Corbard, T., DeRosa, M.L., Genovese, C.R., Gough, D.O., Haber, D.A., Harvey, J.W., Hill, F., Howe, R., Korzenik, S.G., Kosovichev, A.G., Leibacher, J.W., Pijpers, F.P., Provost, J., Rhodes, E.J., Schou, J., Sekii, T., Stark, P.B. and Wilson, P.: 1996, *Science*, **272**, 1300
- van der Sluis, A., and van der Vorst, H.A.: 1990, *Linear Algebra and its Applications*, **130**, 257.
- Vorontsov, S.V., Christensen-Dalsgaard, J., Schou, J., Strakhov, V.N., and Thompson, M.J.: 2002, *Science* **296**, 101. doi:10.1126/science.1069190.
- Xu, X.-L., Liow, J.-S., and Strother, S.C.: 1993, *Med. Phys.*, **20**, 1675.